General information of the article
Type of paper: Article
Title: Effects of interactions between transient granular flows and macroscopically rough beds and their implications for bulk flow dynamics

Authors: C. E. Choi and G. R. Goodwin

Author information:
Co-author: C. E. Choi
Assistant Professor, Department of Civil Engineering, The University of Hong Kong, Pokfulam, Hong Kong SAR, China.
Water Bay, Kowloon, Hong Kong.
E-mail: cechoi@hku.hk

Co-author*: G. R. Goodwin
Postdoctoral fellow, Department of Civil Engineering, The University of Hong Kong, Pokfulam, Hong Kong SAR, China.
E-mail: grgoodwin@connect.ust.hk, cegeorge@hku.hk

* Corresponding author

Word count: 6,621 (main text) + 1,474 (appendices)
Abstract: 196
Figures: 11 (main text) + 3 (appendix)
Tables: 2 (main text) + 1 (appendix)

Effects of interactions between transient granular flows and macroscopically rough beds and their implications for bulk flow dynamics

C. E. Choi[1 2] and G. R. Goodwin[1*]

The Department of Civil Engineering; The University of Hong Kong University, HKSAR, China[1]
The University of Hong Kong Shenzhen Institute of Research and Innovation, Nanshan, Shenzhen, China [2]
Corresponding author [*]

Abstract

Steep-creek beds are macroscopically rough. This roughness causes channelised flow material to decelerate and dissipate energy, which are accounted for by depth-averaged mobility models (DMM). However, practical DMM implementations do not explicitly account for grain-scale basal interactions which influence macroscopic flow dynamics. In this study, we model flows using physical tests with smooth and macroscopically rough bases, and hence evaluate Discrete Element Method (DEM) and DMM models. A scaling effect is identified relating to roughened beds: increasing the number of grains per unit depth tends to suppress dispersion, such that small-scale flows on smooth beds resemble large-scale flows on roughened beds, at least in terms of bulk density. Furthermore, the DEM shows that rougher beds reduce the peak bulk density by up to 15% compared to a smooth bed. Rough beds increase the vertical momentum transfer tenfold, compared to smooth ones. The DMM cannot account for density change or vertical momentum, so DMM flow depths are underestimated by 90% at the flow front and 20% in the body. The Voellmy model implicitly captures internal energy dissipation for flows on rough beds. The parameter ξ can allow velocity reductions due to rough beds observed in the DEM to be captured.

Keywords: landslides, rough beds, depth-averaged model, discrete element model

1. Introduction

Numerically modelling steep-creek hazards such as debris flows and rock avalanches is helpful for assessing whether downstream facilities are at risk, and for designing appropriate countermeasures (Hungr 1995, 2008; McDougall 2017; Koo *et al.* 2017, 2018). Current engineering practice often involves using depth-averaged mobility models (DMM) based on the formulations from Savage and Hutter (1989). The DMM can be used to estimate flow mobility and impact pressure on a barrier, both of which require the flow velocity U and the depth H (Kwan 2012).

Versions of the DMM used by engineers generally treat the granular material as a deformable, incompressible continuum (e.g. Savage and Hutter 1989; Hungr 1995; Tai et al. 2001; Pudasaini and Hutter 2003; Kwan and Sun 2006). The governing equations for simple DMM implementations treat the flow as though: (*i*) pressure is hydrostatic, (*ii*) velocity is uniform across the flow depth, and (*iii*) momentum can only be directed in bed-parallel directions. (Correction factors can nonetheless be applied to account for variation of the velocity of the flow with depth.) Furthermore, although in reality channel beds are not planar (see Fig. 1), the macroscopic morphology of the channel must be smoothed for numerical stability.

However, it remains unclear what the effects of these assumptions are on values output for U and H for flows traversing morphologically irregular topography. In fact, morphologically irregular beds should have several effects on flow dynamics, which can be captured by modelling grains discretely:

(i) Enhancing deceleration – rough beds give rise to a higher apparent basal friction angle than smooth beds.

(ii) Allowing downstream momentum to be transferred vertically (see Kumaran and Bharathraj 2013). This reduces flow density, increases the flow depth and reduces flow energy by promoting inelastic collisions between grains (and can be observed in the footage of some of the flow fronts for 'rough bed' tests collected in Iverson *et al.* 2010; see also USGS 2012 and 2016).

(iii) Allowing simultaneous plug/shear behaviour (Iverson 1997) to manifest, which is associated with depth-varying velocity profiles and convection of flow material. (Fig. 2a).

Versions of the DMM used by practising engineers are typically only able to capture deceleration and energy dissipation caused by rough beds. All decelerative forces due to

friction with a rough bed can be lumped into the basal friction coefficient μ_B. As for bed-induced energy dissipation, which physically involves grains colliding inelastically with one another, the Voellmy model (Voellmy 1955, Salm 1993, Hungr 1995) has been adopted for modelling hazards such as debris flows and rock avalanches for capturing "turbulence" (Hungr 2008; McDougall 2017). This "turbulence" can be interpreted as a general term for energy dissipation that depends on velocity.

However, the precise physical link between (*i*) the basal friction coefficient μ_B and the Voellmy coefficient ξ with (*ii*) the actual physical processes caused by a macroscopically irregular bed are unclear. This causes considerable uncertainty for the values of U and H output by DMM analyses. A key unanswered question could be framed as follows: "For engineering purposes, are the boundary interactions caused by a rough bed important enough that flow velocity and depth output by the DMM are underestimated?".

In this study, we compare discrete and continuum approaches to look at flow depth and velocity, and hence investigate the consequences of neglecting certain flow processes caused by basal roughness. The aim is to model dry, coarse granular flows that have some relevance to those found in the field, including rock avalanches and the fronts of fully-developed debris flows (Hungr *et al.* 2014). (Debris flows are documented as having unsaturated fronts comprising the largest grains in the flow when fully developed, e.g. Bardou 2002. This is also implied from pore-pressure measurements of field debris flows presented in McArdell et al. 2007 and Nagl *et al.* 2020).

2. Methodology

2.1: PHYSICAL TESTS

We performed two physical tests with glass spheres using a flume with dimensions of 3.0 × 0.2 × 0.4 m (length × width × height) (Figs. 3a and 3b). The flume has a storage area for granular material. Material is retained by a gate controlled by a pneumatic cylinder. Smooth, transparent acrylic was used for the channel side walls. A grid was superimposed on one side for PIV analysis.

We used two interchangeable baseplates. One baseplate was smooth, whilst the macroscopically rough baseplate was created by gluing mono-sized glass spheres to acrylic boards using epoxy (see the inset of Fig. 3a). The spheres were placed in a hexagonal close packing (HCP) arrangement.

2.1.1: Experimental procedure

We placed 40 kg of approximately monodisperse glass spheres in the storage area. The nominal diameter was 9.8 mm and the size variation of the spheres was ±10 %. Boundary effects due to the channel walls were limited with more than 20 grains across the channel width (see Jop et al. 2005). Spheres were adopted given their well-defined, uniform diameter; bulk assemblies of spheres are almost incompressible (Iverson 2015), so the insertion method made no difference to the initial bulk density.

We then inclined the flume. We subsequently allowed the spheres in the storage area to rearrange and come to rest. We initiated a high-speed camera facing the side of the channel, and then remotely opened the gate, enabling dam-break (see Staron and Hinch 2005; Tannant and Skermer 2015; Ashwood and Hungr 2016; and Leonardi et al. 2019). The purpose of using dam-break is to create a large pressure gradient to drive the flow downstream. Dam-break creates transient flows with distinct properties at the front, body and tail (Ng et al. 2019).

2.1.2: PIV analysis

We used the Matlab implementation of the open-source program OpenPIV (Thielicke and Stamhuis 2014; Thielicke 2020) for computing vectors for the spheres in our physical tests. The program takes pairs of images, sub-divides each image into a grid and then uses cross-correlation to determine how grains have moved between the two frames. The framerate for the high-speed camera was 250 FPS, so pairs of frames were separated by 4 ms. The reference

grid that we superimposed on the side of the flume was used as a reference for distance, allowing the velocity to be calculated.

2.2: NUMERICAL MODELLING: DISCRETE ELEMENT METHOD

The Discrete Element Method (DEM) (Cundall and Strack 1979) is not a practical tool for engineering applications (Bartelt et al. 2012). Nonetheless, we use it because of its ability to explicitly characterise flow properties caused by discrete interactions between grains and a macroscopically rough bed. It should be noted that coupled CFD-DEM models which explicitly consider both liquids and solids have been proposed by Silva et al. (2016), Leonardi et al. (2016) and Shan and Zhao (2014), but the inclusion of a fluid phase is not strictly necessary if hazards such as debris flow fronts or rock avalanches are being modelled.

The DEM models the movement of individual grains according to Newton's laws of motion, whilst interactions between grains and surfaces are mediated through a contact model (see O'Sullivan 2011). As such, the DEM can explicitly model both morphologically rough beds and flow dispersion due to grain contacts.

There is rich precedent for applying the DEM to model granular flows (e.g. Rycroft 2007; Valentino et al. 2008; Teufelsbauer et al. 2009, 2011; Cleary 2010; Salciarini et al. 2010; Ng *et al.* 2013, 2017, 2019; Albaba et al. 2015, 2018; Choi *et al.* 2015; Law *et al.* 2015; Guo and Curtis 2015; Maione et al. 2015; Leonardi et al. 2016, 2019; Marchelli et al. 2020; Goodwin and Choi 2020). In this study, we adopt the open-source DEM package LIGGGHTS (Kloss and Goniva 2010; DCS Computing 2020), which has previously been used for other studies on granular flow dynamics (e.g. Law et al. 2015; Kesseler 2018; Ng et al. 2019; Goodwin and Choi 2020 and Goodwin et al. 2021).

2.2.1: Procedure

For our macroscopically rough bed, we fixed discrete elements in a hexagonal close packing (HCP) arrangement. Figs. 4a and 4b show the numerical setup in this study.

We generated around 30,000 discrete elements with a total mass of around 40 kg within the storage area (Figs. 4a and 4b), matching the configuration used in Choi et al. (2016). We gave the discrete elements a slight size grading of ±10 % (Fig. 4c) to match the physical spheres and to reduce crystallisation effects (Leonardi et al. 2019; Marchelli et al. 2020). Since our physical and DEM grains are the same size, there was no need to use grain upscaling (e.g. Coetzee 2018).

The grains then settled under an applied gravitational field perpendicular to the channel base. The bulk density of the static grains was around 0.6 (as in Silbert et al. 2003). Thereafter, the direction of gravity was changed to simulate inclining the flume, causing the grains to move slightly. After the grains had again come to rest, the plane partitioning the storage area and the channel was removed, as in Leonardi et al. (2019) and Marchelli et al. (2020).

2.2.2: Input parameters

For the DEM model, only the grain-grain friction angle was back-analysed. The value came from a previous back-analysis presented in Ng et al. (2019), using a flume with the same dimensions and using the same glass spheres. We used a Hertzian contact model based on the formulation from Johnson (1985). We determined the interface friction angle using a series of tilt-tests on a glass board (see Pudasaini et al. 2007 and Mancarella and Hungr 2010). The coefficient of restitution (e) was determined experimentally in Ng et al. (2019). We measured the density of the glass (ρ_{glass}) to be 2650 kg/m^3 (see Choi et al. 2016). Rolling resistance is sometimes applied to simulate the effects of grain shape (Wensrich and Katterfeld 2012; Law et al. 2015), but it was set to zero because spheres were being modelled. A summary of the properties adopted is given in Table 1.

2.2.4: Discrete element modelling: scaling and data extraction

Calculations for quantities extracted from the DEM are the same as those described in Ng et al. (2019), but we repeat them in Appendix A for completeness.

2.3: NUMERICAL MODELLING: SAVAGE-HUTTER MODEL

We implemented the depth-averaged Savage-Hutter model described in Hungr (1995), neglecting (*i*) centrifugal acceleration, since the channel bed is flat and (*ii*) mass transfer between the flow and the base, since our discrete beds were fixed. Since our implementation of the depth-averaged Savage-Hutter model does not explicitly model Bagnoldian velocity profiles, we can explore the effects of their absence by comparing output with data from the physical tests and the DEM. It should nonetheless be noted that more advanced Savage-Hutter models have implemented phenomena such as shear/plug behaviour (e.g. Gray and Edwards 2014) or more generally multiple layers (Fernández-Nieto *et al.* 2016). Furthermore, there exist DMM models which consider multiple phases (e.g. Iverson and George 2014 and Bouchut et al. 2016). However, such models have yet to been widely adopted by practicing engineers.

Further details of the DMM implementation are given in Appendix B.

2.4: PHYSICAL AND NUMERICAL TEST PROGRAM

Two physical tests were performed in which the channel inclination was 30° and the flow grain size was 10 mm. The ratios between the flow grain size and the basal grain size δ_B/δ_F were zero and unity. Zero indicates a smooth bed, whilst unity represents a macroscopically rough bed. A further four physical tests were performed using dry gravel to compare against the spheres to check that flow kinematics were qualitatively similar for both cases. Data for these tests using gravel are included in Appendix C.

For the numerical simulations, eight cases were performed using the DEM for a range of flow and basal grain sizes. Sixteen cases were run using the DMM for a range of frictional parameters and the Voellmy coefficient ξ (covering the value of 500 m/s^2 used in some design guidelines; see Kwan 2012). The bulk density ρ was set at 1650 kg/m^3. Both physical and numerical tests are summarised in Table 2.

3. Comparison of physical and numerical models

In Fig. 5, parts (a) and (b) show physical flow dynamics for δ_B/δ_F of zero (a smooth bed) and unity (a macroscopically rough bed). Parts (c) and (d) show computed flow dynamics for the same ratios of δ_B/δ_F. Part (e) shows dynamics for the DMM for a smooth bed (i.e. δ_B/δ_F of zero, corresponding to a smooth bed with a physically measured basal roughness of 11°). For each case, the viewpoint is centred at an x-position of 1.55 m from the gate and has a field of view of 0.5 m.

Fig. 5a(*i*) (at t = 0.0 s), shows the flow incoming from the left. The flow front is one to three grain diameters deep. The flow is relatively dense and coherent, consistent with flows on smooth beds presented in Gray et al. (2003), Pudasaini et al. (2007), Choi et al. (2016) and Ng et al. (2019). At t = 0.1 s (Fig. 5a(*ii*)), the body of the flow is around five grain diameters deep; this depth is maintained for the rest of the flow (Figs. 5a(*iii*) to (*vi*)).

In Figs. 5b(*i*) and 5b(*ii*), where t = 0.0 and 1.0 s respectively, the flow front is much more dispersed and discrete. Frontal grains saltate to heights of more than 25 grain diameters, and it is difficult to identify the front clearly. At t = 0.2 to 0.5 s (Figs. 5b(*iii*) to 5b(*vi*)), the body is more coherent than the head. The flow depth is greater than for the smooth bed (c.f. Fig. 5a). Saltation over the flow body is more apparent than for the smooth case.

Figs. 5c and 5d show DEM simulations that correspond to back-analyses of Figs. 5a and 5b respectively. Fig. 5c shows that the overall flow kinematics are captured very closely (as per Ng et al. 2019). Additionally, the colour legend, which shows velocity, indicates that the velocity is almost constant along the depth of the flow – the entire mass appears to tend towards being a "plug flow" (see Iverson 1997), although the rigorous definition of "zero shear between layers" is not fulfilled. In contrast, the colour-legend of Fig. 5d shows a clear gradation in velocities across the depth of the flow, implying that the rough bed has caused the emergence of a "shear zone" (Anderson and Jackson 1992; Jenkins and Askari 1994; Iverson 1997). However, whilst the flow front is well-captured for the rough bed, there is more saltation over the body of the flow than in the physical experiment.

Fig. 5e shows the flow dynamics for the DMM. The parameters adopted for this simulation were a basal roughness of 11° and a Voellmy coefficient ξ of 25 m/s^2, both of which were adopted to try to match the observed flow kinematics for the flows on the smooth base.

Chalk et al. (2017) have previously noted that values of ξ of around 20 m/s^2 give closer results to small-scale modelling approaches, in contrast to back-analysed values for prototype flows that are at least an order of magnitude higher. For instance, Schraml *et al.* (2015) back-

analysed a value of around 200 m/s^2 to back-analyse debris flow events. Recommended values in Kwan (2012) are of the same order of magnitude as Schraml *et al.* (2015). The flow dynamics are broadly similar to the other two smooth bed cases. Increasing ξ would mean that the DMM flow would be slower and thicker, which could be postulated to give a better match with the physically observed flow kinematics for the smooth bed case. A fuller investigation of ξ is given in Figs. 9 to 11.

The flow dynamics from the DMM are broadly similar to the other two smooth bed cases (i.e. from the physical test and the DEM simulation). The DMM is not able to achieve flow kinematics reminiscent of the rough bed condition of $\delta_B/\delta_F = 1$. This is because although the flow front should have a low bulk density, the density is fixed in the DMM. The bulk density ρ was set according to the at-rest bulk density of an array of glass spheres, i.e. 1650 kg/m^3. This parameter could be adjusted to try to better match the observed flow kinematics, especially if a relationship were developed allowing it to change along the length of the flow, although such modifications to the DMM are outside the scope of this study.

Appendix C contains complementary figures showing the dynamics of gravel on smooth and rough beds. Similar dispersed flow fronts are observed for the gravel, although the degree of dispersion is less than for the flows of glass beads. This lends confidence to the adoption of glass beads in terms of being able to capture the same basic mechanisms as coarse geological materials.

Results from Fig. 5 preliminarily suggest that engineers need to be aware that rough beds can cause very dispersed flow fronts, with material saltating unpredictably, at least for the nominal ratio of h/δ considered in these tests (up to h/δ of 5 as measured from the cases using a smooth bed).

4. Interpretation of results

4.1 ABILITY OF DEM TO CAPTURE PROTOTYPE FLOW MECHANISMS

In this section, we look at output from the DEM only, to assess whether shear/plug flows (see Iverson 1997) can be reproduced at small-scale using a discrete model.

4.1.1 Solid volume fraction (DEM)

Figs. 6a and 6b show the change in the solid volume fraction along the length of the flow on the ordinate and the position along the length of the flow on the abscissa. Two cases are shown: (a) δ_F = 10 mm and (b) δ_F = 20 mm. The value for randomly packed, uniformly-sized spheres from Silbert et al. (2003) is also shown here for reference.

In Fig. 6a, for δ_B/δ_F = 0.00 (a smooth bed), the solid volume fraction rapidly increases from zero at the flow front to about 0.5 in the body and 0.4 at the tail. The trend is consistent with results from Dent et al. (1998), Bugnion et al. (2013) and Ng et al. (2019), where the flow front density was less than in the body. Progressively roughening the bed reduces the peak solid volume fraction attained for each flow. For instance, the maximum value for δ_B/δ_F = 0.25 is 0.50; whereas for δ_B/δ_F = 1.00, the peak is 0.40.

Increasing the size of the basal grains increases the dispersive stress (Bagnold 1954), according to:

$$P = a_i \sigma \lambda f(\lambda) \delta^2 \left(\frac{dU}{dz}\right)^2 \cos \alpha_i \quad (1)$$

where a_i is a proportionality constant; σ is the normal stress; λ is the linear concentration; δ is the grain size; U is the granular velocity; the term dU/dz has the physical meaning of shear strain; and α_i is an angle relating to collisions of grains. The increase of the dispersive stress occurs because the range of scattering angles α_i increases, which reduces the bulk density, which tends to cause momentum to be directed away from the channel base.

Increasing the flow grain size, as shown in Fig. 6b, causes the solid volume fraction to decrease for the same ratio of grain sizes for the flow and the bed. There are fewer grains across the depth of the flow. As such, less energy is expended through inelastic collisions, so grains can saltate higher.

Fig. 6c shows the same ratio of δ_B/δ_F = 1 for two different scales: Ω = 1 and 2, where Ω is a geometric scaling factor applied to the dimensions of the flume and the total volume of the material. Doubling Ω means that the volume of both the flume and the total volume of granular material increases by eight times. δ_F is held constant at 10 mm for each value of Ω, so

the number of grains increases by eight times too. Meanwhile, the ratio h/δ changes from a nominal value of around 5 for $\Omega = 1$ to 10 for $\Omega = 2$ (based on the small-scale flows shown in Fig. 5). Increasing h/δ tends to cause the bulk volume fraction of the flow material to become more (but not completely) suppressed. This implies that for steep creek hazards with dry, coarse granular fronts–such as debris flows or rock avalanches–the flow front may be highly dispersed, especially for small nominal values of h/δ (e.g. $h/\delta < 5$). Furthermore, the governing parameter for whether practical implementations of the DMM can capture the bulk behaviour of flows on morphologically rough beds appears to be h/δ, which varies depending on boulder size and concentration. For flows with large values of h/δ (up to 2,000; see Iverson 1997), it appears that small-scale flows on smooth beds resemble large-scale flows on roughened beds, at least in terms of the bulk density, although other aspects such as the velocity profile may still differ. (This is discussed further in the interpretation of Fig. 8.)

Figs. 6a to 6c serve as a useful point of reference for engineers using depth-averaged models for estimating impact pressure, since even for flows on smooth beds, the solid volume fraction is much lower at the front that in the body. Engineers need to account for this when designing barriers to resist impact from flow fronts, since the bulk density is a governing parameter for impact force (see Vagnon and Segalini 2016, Song et al. 2017 and Ng et al. 2018):

$$F_{\text{impact}} \propto \int_0^H \rho U^2 \, dh \tag{2}$$

where H is the flow depth. Nonetheless, to get a conservative value for the impact pressure, it would be acceptable to assume the at-rest density. Furthermore, engineers should be aware that the earth pressure coefficient (Hungr 1995; Kwan and Sun 2006) may not be applicable to the highly dispersed flow fronts that are caused by macroscopically rough beds: inter-grain contact stresses are very short-lived. As such, the driving pressure gradient at the flow front is caused by a different mechanism (inelastic collisions), which is not captured by the DMM.

4.1.2 Direction of momentum (DEM)

Depth-averaged models do not explicitly consider vertical momentum transfer. Vertical momentum transfer involves macroscopically rough beds reorienting downstream momentum away from the channel base. (See also Gioia et al. 2006 and Hsu et al. 2014).

Fig. 7 shows P_{norm} (Eqn. A5) on the ordinate and L (Fig. A1) on the abscissa. All three parts of the graph show that increasing the macroscopic basal roughness (i.e. δ_B/δ_F) increases the proportion of grain momentum directed in the z-direction.

Furthermore, the z-direction momentum appears to increase with grain size for a given ratio of δ_B/δ_F. This is because for smaller grains, there are more grains throughout the flow depth for a given total volume of material. This means that more inelastic collisions can take place throughout the depth of the flow, thus tending to dissipate energy, consistent with results for the solid volume fraction. This trend is maintained for flows traversing rough beds, although the differences are less pronounced.

Fig. 7 gives a rough indication of when the bed condition might reduce the feasibility of a depth-averaged approach. As the vertical component of momentum increases past 10%, depth-averaged approaches progressively overestimate the downstream component of momentum as well as density, whilst simultaneously underestimating flow depth, as shown in previous graphs.

4.1.3 Velocity profile and Savage number (DEM)

Fig. 8 shows velocity profiles and Savage number profiles for two cases. Both are important parameters for scaling granular flows (see Iverson 1997 and Silbert et al. 2001). They can be used to identify whether models at different scales are able to capture the same flow processes. Fig. 8a is for a smooth bed ($\delta_B/\delta_F = 0$) and Fig. 8b is for a rough bed ($\delta_B/\delta_F = 1$). Different lines correspond to different points along the length of the flow; we select $L = 0.25$, 0.50 and 0.75. (The velocity and Savage profiles are not readily quantifiable for $L = 0.00$ and $L = 1.00$ given the high degree of dispersion.)

Fig. 8a(*i*) shows that the velocity of the flow on a smooth bed is almost constant along the depth of the flow for each of the three points sampled. Fig. 8a(*ii*) shows that the Savage number remains under 0.1 over the entire depth, indicating that frictional stresses dominate. This appears to give rise to behaviour that is somewhat similar to a plug flow (see Iverson 1997), with minimal shearing between layers. (It should be noted that a common definition of "plug flow" involves zero shearing between layers, and that frictional flows are not by definition plug-like.) The variation of the Savage number with depth is consistent with the velocity profile.

In contrast, in Fig. 8b(*i*), the velocity at the base of the flow is about half that at the top. This type of shear profile is more characteristic of flows in the field (Nagl et al. 2020) than those on the smooth bed, implying that macroscopically rough beds are essential for modelling realistic velocity profiles. The profile of the Savage number (Fig. 8b(*ii*)) shows that the bottom half of the flow is in a collisional regime, whilst the top half is in a frictional regime. The ratio of the heights of the two regimes is different to that qualitatively proposed by Iverson (1997)

for plug and shear regions. This is likely related to the low stress levels in our flows. For a scaled-up flow, it is expected that the collisional region would undergo a relative decrease in size, following the increased solid volume fraction shown in Fig. 6c.

Fig. 8 shows that the DEM model appears to be capable of capturing both shear and plug-like regions that are characteristic of prototype steep-creek hazards, at least on a qualitative level. Velocity profiles reminiscent of prototype flows, specifically Bagnoldian profiles that tend towards a no-slip condition at the base (Gioia et al. 2006), are evidently also capturable using the DEM. Such velocity profiles are conditional on beds which are macroscopically rough.

4.2 COMPARISON OF DISCRETE AND CONTINUUM OUTPUT

Calculating the impact force on an obstacle (Eqn. 2) due to steep-creek hazards such as debris flows or rock avalanches is one of the ultimate goals of using numerical approaches. The flow depth and velocity are calculable from both discrete and depth-averaged models. Effects on the flow depth and velocity due to basal roughness that are not capturable using the depth-averaged approach can be highlighted by comparing output with that from the DEM.

4.2.1 Flow depth (DEM and DMM)

Fig. 9 shows the depth of the flow at (a) the front, (b) the body and (c) the tail of various flows from the DEM and DMM. Output from the DEM includes two flow grain sizes: 10 mm and 20 mm; and four ratios of grain sizes in the flow and the base. For the depth-averaged method, four basal friction angles μ_B are considered, based around the tilt tests described in the methodology.

Fig. 9a shows that the depth at the flow front in the DEM increases as the morphological basal roughness is increased. This indicates that progressively morphologically rougher (i.e. bumpier) beds become more efficient at redirecting downstream momentum in other directions, consistent with the results shown in Fig. 7. The DMM is unable to capture the extreme flow depth at the front because (*i*) the density is assumed to be fixed (Hungr 1995) and (*ii*) the DMM implementation used in this study does not include an equation for capturing the upwards transfer of momentum. Engineers should thus be aware that material at the flow front could be spraying at a higher height than predicted by the DMM. This has implications for flows going around bends (e.g. Scheidl et al. 2014), where they could spill out and move downstream in unexpected directions. Additionally, barriers should be designed to avoid overspilling from very loose, collisional flow fronts.

The depth of material in the flow body is more consistent between the DEM and the DMM (Fig. 9b). However, the trend of the flow depth increasing or decreasing with the increase in basal friction (changed using μ_B in the DMM and the basal grain size in the DEM) differs. The thickness for the DEM increases with macroscopic basal roughness. This is because of the upward transfer of momentum which makes the flow less dense (Fig. 6). This effect also occurs at the flow front, but to a much greater extent.

In contrast, increasing the basal roughness for the DMM slows the flow down and allows the earth pressure to relax more over a given distance, causing a slight net decrease in the flow depth. For a given Voellmy coefficient ξ, this tends to cause the flow depth to be overestimated for smooth beds, and underestimated for progressively rougher beds. This means that for field conditions – where beds tend to be macroscopically rough (Fig. 1) – the depth of the flow body may be underestimated.

Using higher values for flow depths is considered to be more conservative as per current design guidelines such as Kwan (2012), which recommend adopting the maximum flow depth for the calculation of impact force. Fig. 9b shows that lower values of ξ tend to increase the flow depth. (Note: we interpret a lower value of the Voellmy coefficient ξ as enabling more dissipation of energy due to frictional shearing and inelastic collisions.) Flow depths are higher because of the dependence of ξ on the flow velocity (Hungr 1995). Lower values of ξ cause a strong braking force on the flow as soon as the boundary blocks start to accelerate, limiting the strain between boundary blocks. This means that the mass blocks tend not to decrease in height as much, since mass must be conserved.

Fig. 9c shows that the DMM, in addition to being unable to capture the depth profile at the flow front, is also unable to do so at the rear of the flow, and for the same reasons. Loose saltating debris may thus be present at the tail of a flow, which could be an issue for debris flows with small volumes. Flows impacting rigid barriers typically pile up and form a ramp (e.g. Faug et al. 2002); loose material at the tail of the flow may be able to saltate up and over the barrier.

Overall, engineers should be aware that for dry, coarse flows (such as rock avalanches or the fronts of debris flows) traversing macroscopically rough beds, the uncertainty in flow depth for the DMM can be very large at the front and tail, at least for the range of h/δ considered in this study (nominally $h/\delta < 5$ for the flows on smooth beds in this study). The flow depth from the DMM is up to 90 % and 250 % less than the DEM, respectively. The uncertainty for the flow depth in the body is less, with output from the DMM being up to 20 % less than the

DEM. Furthermore, the reduction in density that is not accounted for in the DMM (see Fig. 6) may not completely offset the underestimate of the flow depth for the purposes of calculating impact force.

4.2.2 Flow velocity (DEM and DMM)

Fig. 10 shows the flow velocity as a function of basal roughness. For the DEM, only a single grain size (10 mm) is shown for clarity; the velocities for the 20 mm grains are almost identical and are omitted. For the DMM, four values of the Voellmy coefficient ξ are shown, covering the range of actual coefficients adopted by engineers (Kwan 2012).

Fig. 10a shows that somewhat counterintuitively, the frontal flow velocity actually increases as the macroscopic roughness of the base (δ_B/δ_F) increases. This is because for rough beds, the grains at the flow front are barely in contact with the base. As such, energy is mostly lost through inelastic collisions, rather than continuous frictional shearing. Regardless of the value of ξ selected, the DMM is not able to capture this increase in frontal velocity. This is because the basal friction and ξ are not linked with what type of energy dissipation is occurring (i.e. frictional shearing or inelastic collisions), and assume both types of energy dissipation to be present continuously. This is why the DMM shows a different, downwards trend, when compared to the DEM.

Additionally, it is interesting to note that larger values of ξ, indicating low dissipation of energy due to internal flow processes, give better matches for the frontal velocity. This is consistent with the above observation of how grains at the flow front tend to behave, where they saltate and have limited contact with the base. Values of the Voellmy coefficient ξ appropriate for the flow velocity are opposite to the depth, with smaller values of ξ yielding higher velocities; there is a clear trade-off between the two effects. Given the squared velocity (U^2) term in the equation for impact force (Eqn. 2), as opposed to the unindexed depth term (H), adopting a higher value of ξ should lead to a higher predicted impact force.

This notwithstanding, engineers should be aware that the frontal velocity computed using the DMM may nonetheless be an underestimate, especially if the flow includes boulders that are moving discretely. This is because resisting forces due to basal friction may be low or zero. The velocity term adopted for calculating impact force should be revised accordingly.

4.2.3 Froude number

Fig. 11 shows *Fr* on the ordinate and the position along the flow length (*L*) on the abscissa. *Fr* is given by (Armanini 2015; Armanini *et al.* 2014):

$$Fr = \frac{U}{\sqrt{gH\cos\theta}} \tag{3}$$

Two bed conditions for a single grain size (10 mm) are shown for the DEM tests; the Froude profile for the 20 mm grains is qualitatively very similar and are omitted for clarity. Two pairs of lines are shown for the DMM showing the effects of the basal friction angle and the Voellmy coefficient ξ. The threshold for supercritical flows ($Fr > 10$) and a transitional zone ($0.1 < Fr < 10$) in which both sub- and supercritical characteristics manifest (Faug 2015) are shown for reference. Subcritical flows fall in the range ($0 < Fr < 0.1$) (Faug 2015). Subcritical flows are not considered because they are usually not an important case for impact.

The Froude number for the DEM smooth bed starts at around 12.5, decreases to a minimum of around 6.0 in the body of the flow, and then increases again to 12.0 at the tail of the flow. This is qualitatively consistent with results from Ng et al. (2019). The change in *Fr* is mostly due to the arc-sharped profile of the flow (Fig. 5), which causes a constantly-changing depth.

For the DEM simulation on the macroscopically rough bed ($\delta_B/\delta_F = 1$), the profile is qualitatively similar for the front and body of the flow. The starting value of *Fr* is much lower at 7, after which it drops to around 3 in the body. The end of the tail is different to the smooth bed, since *Fr* drops again. This is because most of the downstream momentum is transferred away from the slope, simultaneously reducing the downstream velocity and increasing the depth. It should also be noted that *Fr* is an average value taken over the depth of the flow. However, given the velocity profiles already shown in Fig. 8, it should be clear that the average value is reduced by the slower-moving grains near the base. This suggests that the presence of both shear and plug layers (Iverson 1997; Fig. 2a) also tends to reduce *Fr*, compared to plug flows on a smooth bed.

The *Fr* profile obtained from the DMM for $\mu_B = 11°$ is similar to that from the DEM for the smooth bed, assuming that there is little energy dissipation due to internal processes. (In other words, when ξ is set to be near to the value of 500 m/s^2 used in current design guidelines; see Kwan 2012). Increasing the basal friction angle to 21° allows the DEM to broadly capture the *Fr* profile of the DEM flow on the rough bed. However, the DMM overestimates *Fr* at the front and at the tail, because it underestimates the depth of the flow (see Fig. 9). Decreasing ξ to 25 m/s^2 causes *Fr* to become significantly underestimated. It has already been seen that a low value of ξ gives higher flow depths but lower velocities. Since the

depth term in the Froude number is square rooted (Eqn. 3), the velocity dominates, so a higher value of ξ gives a better match with the DEM.

A further implication can be collectively obtained from Figs. 9 to 11. Specifically, values quoted for *Fr* for prototype steep-creek hazards, such as $0 < Fr < 5$ for debris flows (Hübl et al. 2009) or $5 < Fr < 10$ for snow avalanches (Sovilla et al. 2008) may not be applicable to the entire length of flows. Nonetheless, the flows modelled in this study do give values of *Fr* that overlap with these ranges from the literature.

4.3 Discussion on flows including viscous pore fluid

For coarse granular flows such as the fronts of debris flows or rock avalanches, interstitial liquids are unlikely to have a substantial influence on the development of flow fronts because the permeability is very high. This implies that the timescale for dissipation of excess pore pressure should be very short. This can partly be quantified using one of the dimensionless numbers proposed in Iverson (1997):

$$N = \frac{\dot{\gamma}\mu\delta^2}{\nu_{\mathrm{sol}} k_{\mathrm{perm}} E_{\mathrm{bulk}}} \tag{4}$$

where $\dot{\gamma}$ is the shear rate; μ is the fluid dynamic viscosity; δ is the grain diameter; ν_{sol} is the solid volume fraction; k_{perm} is the permeability; and E_{bulk} is the bulk elastic modulus (which is inversely proportional to the bulk stiffness). Higher values of *N* suggest the timescale for pore pressure dissipation across the distance δ dominates, whilst lower values imply the timescale for pore pressure generation due to granular interactions dominates. In other words, high values of *N* imply that pore pressure generation is unlikely to influence the flow dynamics. For extremely loose flow fronts, the bulk elastic modulus should be extremely low, and cause relatively high values of *N*. Large-scale tests using mixtures of gravel and fluids show that the gravel tends to separate from the rest of the flow material, thus not being affected by pore pressures due to interstitial liquid. (See USGS 2012 and 2016, which show that the frontal coarse grains are dry, with a liquid surge following.) This is further supported by observations in McArdell et al. (2007) that the flow front is mostly unsaturated.

5. Conclusions

In this study, we set out to answer the following question: "For engineering purposes, are the boundary interactions caused by a rough bed important enough that flow velocity and depth output by the DMM are underestimated?"

To address this question, we performed physical tests using both macroscopically smooth and macroscopically rough beds and then validated a DEM model. It was found that the DEM can capture mesoscopic behaviour, specifically a shear zone and a rigid (Iverson 1997). We then compared results with those from an implementation of the depth-averaged Savage-Hutter model (DMM) similar to those commonly employed in engineering practice (Hungr 1995).

Key conclusions are as follows:

1) A scaling effect is identified relating to roughened beds: increasing the number of grains per unit depth h/δ tends to suppress dispersion, such that small-scale flows on smooth beds resemble large-scale flows on roughened beds, at least in terms of bulk density. This implies that the governing parameter for whether practical implementations of the DMM can capture the bulk behaviour of flows on morphologically rough beds is h/δ, which varies depending on boulder size and concentration. A small degree of basal roughness is nonetheless recommended for small-scale experimental campaigns to allow the development of realistic velocity profiles without causing flows to become overly dispersed, although the exact degree of roughness required depends on material and scale.
2) Rougher beds cause the peak bulk density to be up to 15% less than on a smooth bed. Macroscopically rough beds can also cause more than ten times the vertical momentum for rough beds than smooth beds. Since the DMM cannot account for density change or vertical momentum, the DMM underestimates the flow depth by up to 90% at the flow front, around 20% in the body and up to 250% at the tail.
3) The Voellmy model can be assumed to implicitly simulate internal energy dissipation due to frictional shearing and inelastic collisions. Assuming that the maximum depth and velocity in a flow should be adopted for conservatism (as per Kwan 2012), high energy dissipation in the DMM gives the largest flow depths and low dissipation gives the highest velocities. Since velocity dominates impact pressure (being squared), dissipation coefficients that yield low energy dissipation ($\xi = 625$ m/s^2) best matched the reduced-scale DEM simulation results.
4) The frontal flow velocity for discrete grains increases as the macroscopic roughness

increases. This is because grains mainly dissipate energy through occasional inelastic collisions with the base, rather than continuously frictionally shearing against it. The DMM cannot capture this mechanism as the basal friction term assumes constant contact at the base. Engineers should be aware that frontal velocities output by the DMM may be underestimates.

6. Acknowledgements

The authors are thankful for the funding from the National Natural Science Foundation of China (51709052), as well as the Research Grants Council of Hong Kong (General Research Fund Grant 27205320, 16212618, 16210219, Area of Excellence GRANT AoE/E-603/18 and Theme-based Research grant: T22-603/15N). The authors are also grateful for the support from the start-up grant provided by the Faculty of Engineering at the University of Hong Kong.

7. References

Albaba, A., Lambert, S., Nicot, F., and Chareyre, B. 2015. Relation between microstructure and loading applied by a granular flow to a rigid wall using DEM modelling. Granular Matter, **17**(5): 603–616.

Albaba, A., Lambert, S., and Faug, T. 2018. Dry granular avalanche impact force on a rigid wall: analytic shock solution versus discrete element simulations. Physical Review E, **97**: 052903.

Ancey, C. 2001. Dry granular flows down an inclined channel: experimental investigations on the friction-collisional regime. Physical Review E, **65**: 011304.

Anderson, K. G., and Jackson, R. 1992. A comparison of some proposed equations of motion of granular materials for fully developed flow down inclined planes. Journal Fluid Mechanics, **241**: 145–168.

Ashwood, W., and Hungr, O. 2016. Estimating total resisting force in flexible barrier impacted by a granular avalanche using physical and numerical modelling. Canadian Geotechnical Journal, **53**: 1700–1717.

Armanini, A., Larcher, M., and Odorizzi, M. 2011. Dynamic impact of debris flow front against a vertical wall. In: Proceedings of the 5th International Conference on Debris-Flow Hazards Mitigation: Mechanics, Prediction and Assessment 2011, p. 1041–1049.

Armanini, A. 2013. Granular flows driven by gravity. Journal of Hydraulic Research, **51**(2): 111–120.

Armanini, A., Larcher, M., Nucci, E., and Dumbser, M. 2014. Submerged granular channel flows driven by gravity. Advances in Water Resources, **63**: 1–10.

Armanini, A. 2015. Closure relations for mobile bed flows in a wide range of slopes and concentrations. Advances in Water Resources, **81**: 75–83.

Bagnold, R. A. 1954. Experiments on a gravity-free dispersion of large solid spheres in a Newtonian fluid under shear. Pr.ceedings of the Royal Society A, **225**: 49–63.

Bardou, E. 2002. Methodologie de diagnostic des laves torrentielles sur un bassin versant alpin. PhD Thesis, École Polytechnique Fédérale de Lausanne, Switzerland.

Bartelt, P., Bühler, Y., Buser, O., Christen, M. and Meier, L. 2012. Modelling mass-dependent flow regime transitions to predict the stopping and depositional behavior of snow avalanches. Journal of Geophysical Research, **117**: F01015.

Bouchut, F., Fernández-Nieto, E. D., Mangeney, A. and Narbona-Reina, G. 2016. A two-phase two-layer model for fluidized granular flows with dilatancy effects. Journal of Fluid Mechanics, **801**: 166–221.

Bugnion, L., Schaefer, M., and Bartelt, P. 2013. Density variations in dry granular avalanches. Granular Matter, **15:** 771–781.

Chalk, C., Pastor, M., Borman, D., Sleigh, A., Peakall, J., Murphy, W. and Fuentes, R. 2017. A smoothed particle hydrodynamics study of an experimental debris flow. In 4th World Landslide Forum 2017, Ljubljana, Slovenia, EU, pp. 573–578.

Choi, C. E., Ng, C. W. W., Law, R. P. H., Song, D., Kwan, J. S. H., and Ho, K. K. S. 2015. Computational investigation of baffle configuration on impedance of channelized debris flow. Canadian Geotechnical Journal, **52**(2): 182–197.

Choi, C. E., Goodwin, G. R., Ng, C. W. W., Cheung, D. K. H., Kwan, J. S. H., and Pun, W. K. 2016. Coarse granular flow interaction with slit-structures. Géotechnique Letters, **6**: 267–274.

Cleary, P. W. 2010. DEM prediction of industrial and geophysical particle flows. Particuology, **8**: 106–118.

Coetzee, C. J. 2018. Particle upscaling: calibration and validation of the discrete element method. Powder Technology, **344**: 487–503.

Cundall, P. A., and Strack, O. D. L. 1979. A discrete numerical model for granular assemblies. Géotechnique, **29**(1): 47–65.

DCS Computing. 2020. LIGGGHTS User Manual (online). URL: https://www.cfdem.com/media/DEM/docu/Manual.html. (Accessed on 08/03/2020).

Dent, J. D., Burrell, K. J., Schmidt, D. S., Louge, M. Y., Adams, E. E., and Jazbutis, T. G. 1998. Density, velocity and friction measurements in a dry-snow avalanche. Annals of Glaciology, **26**: 247–252.

Faug, T., Lachamp, P., and Naaim, M. 2002. Experimental investigation on steady granular flows interacting with an obstacle down an inclined channel: study of the dad zone upstream from the obstacle Application to interaction between dense snow avalanches and defense structures. Natural Hazards and Earth System Sciences, **2**: 187–191.

Faug, T. 2015. Macroscopic force experienced by extended objects in granular flows over a very broad Froude-number range. European Physics Journal E, **38**(5): Article 34.

Fernández-Nieto, E. D., Garres-Díaz, J., Mangeney, A. and Narbona-Reina, G. 2016. A multilayer shallow model for dry granular flows with the μ(I)-rheology: application to granular collapse on erodible beds. Journal of Fluid Mechanics, **798**: 643–681.

Gioia, G. Ott-Monsivais, S. E. and Hill, K. M. 2006. Fluctuating velocity and momentum transfer in dense granular flows. Physical Review Letters, **96**: 138001.

Goodwin, G. R. (2018). Unsteady dry granular flow interaction with slit-structures. PhD Thesis, Hong Kong University of Science and Technology, Hong Kong SAR, China.

Goodwin, G. R. and Choi, C. E. 2020. Slit structures: Fundamental mechanisms of mechanical trapping of granular flows. Computers and Geotechnics**, 119**: 103376.

Goodwin, G. R. Choi, C. E. & Yune, C.-Y. 2021. Towards rational use of baffle arrays on sloped and horizontal terrain for filtering boulders. *Canadian Geotechnical Journal* (accepted).

Gray, J. M. N. T., Tai, Y. C., and Noelle, S. 2003. Shock waves, dead-zones and particle-free regions in rapid granular free-surface flows. Journal of Fluid Mechanics, **491**: 161–181.

Gray, J. M. N. T., and Edwards, A. N. 2014. A depth-averaged mu(I)-rheology for shallow granular free-surface flows. Journal of Fluid Mechanics, **755**: 503–534.

Guo, Y., and Curtis, J. S. 2015. Discrete element method simulations for complex granular flows. Annual Review of Fluid Mechanics, **47**: 21–46.

Hsu, L., Dietrich, W. E. and Sklar, L. S. 2014. Mean and fluctuating basal forces generated by granular flows: laboratory observations in a large vertically rotating drum. JGR Earth Surface, **119**(6): 1283–1309.

Hübl, J., Suda, J., Proske, D., Kaitna, R., and Scheidl, C. 2009. Debris flow impact estimation. In Proceedings of the 11th International Symposium on Water Management and Hydraulic Engineering, Ohrid, Macedonia, 1–5 September 2009. pp. 137–148.

Hungr, O. 1995. A model for the runout analysis of rapid flow slides, debris flows and avalanches. Canadian Geotechnical Journal, **32**: 610–623.

Hungr, O. 2008. Numerical modelling of the dynamics of debris flows and rock avalanches. Geomechanics and Tunnelling, **2**: 112–119.

Hungr, O., Leroueil, S. and Picarelli, L. 2014. The Varnes classification of landslide types, an update. Landslides, **11**: 167–194.

Iverson, R. M. 1997. The physics of debris flows. Reviews of Geophysics, **35**(3): 245–296.

Iverson, R. M., Logan, M., LaHusen, R., and Berti, M. 2010. The perfect debris flow? aggregated results from 28 large-scale experiments. *Journal of Geophysical Research: Earth Science*, **115**: F03005. DOI: 10.1029/2009JF001514.

Iverson, R. M., and George, D. L. 2014. A depth-averaged debris-flow model that includes the effects of evolving dilatancy. I. Physical basis. Proceedings of the Royal Society A: Mathematical, Physical and Engineering Sciences, **470**: 20130819.

Iverson, R. M. 2015. Scaling and design of landslide and debris-flow experiments. Geomorphology, **244**: 9–20.

Jenkins, J. T., and Askari, E. 1999. Hydraulic theory for a debris flow supported by a collisional shear layer. Chaos, **9**(3): 654–58.

Johnson, K. L. 1985. Contact mechanics. Cambridge University Press, London, UK.

Jop, P., Forterre, Y., and Pouliquen, O. 2005. Crucial role of sidewalls in granular surface flows: consequences for the rheology. Journal of Fluid Mechanics, **541**: 167–192.

Kesseler, M., Heller, V., and Turnbull, B. 2018. A laboratory-numerical approach for modelling scale effects in dry granular slides. Landslides, **15**: 2145–2159. DOI: 10.1007/s10346-018-1023-z.

Kloss, C., and Goniva, C. 2010. LIGGGHTS – a new open source discrete element simulation software. In Proceedings of the 5th International Conference on Discrete Element Methods. pp. 25–26.

Koo, R. C. H., Kwan, J. S. H., Lam, C., Ng, C. W. W., Yiu, J., Choi, C. E., Ng, A. K. L., Ho, K. S. S., and Pun, W. K. 2017. Dynamic response of flexible rockfall barriers under different loading geometries. Landslides, **14**: 905–916.

Koo, R. C. H., Kwan, J. S. H., Lam, C., Goodwin, G. R., Choi, C. E., Ng., C. W. W., Yiu, J., Ho, K. K. S., Pun, W. K. 2018. Back-analysis of geophysical flows using 3-dimensional runout model. Canadian Geotechnical Journal, **55**(8)**:** 1081–1094. DOI: 10.1139/cgj-2016-0578.

Kumaran, V., and Bharathraj, S. 2013. The effect of base roughness on the development of a dense granular flow down an inclined plane. Physics of Fluids, **25**: 070604.

Kwan, J. S. H. and Sun, H. W. 2006. An improved landslide mobility model. Canadian Geotechnical Journal, **43**(5): 531–539.

Kwan, J. S. H. 2012. Guidance on design of rigid debris-resisting barriers. GEO Report No. 270. Geotechnical Engineering Office, Civil Engineering and Development Department, the Government of the Hong Kong Special Administrative Region.

Law, R. P. H, Choi, C. E., and Ng, C. W. W. 2015. Discrete element investigation of the influence of granular debris flow baffles on rigid barrier impact. Canadian Geotechnical Journal, **53**(2): 179–185.

Leonardi, A., Wittel, F. K., Mendoza, M., Vetter, R., and Herrmann, H. J. 2016. Particle–fluid–structure interaction for debris flow impact on flexible barriers. Computer-Aided Civil and Infrastructure Engineering, **31**(5): 323–333.

Leonardi, A., Goodwin, G. R., and Pirulli, M. 2019. The force exerted by granular flows on slit-dams. Acta Geotechnica, **14**: 1949–1963. DOI: 10.1007/s11440-019-00842-6.

Maione, R., De Richter, S. K., Mauviel, G., and Wild, G. 2015. DEM investigation of granular flow and binary mixture segregation in a rotating tumbler: influence of particle shape and internal baffles. Powder Technology, **286**: 732–739.

Mancarella D. and Hungr O. 2010. Analysis of run-up of granular avalanches against steep, adverse slopes and protective barriers. Canadian Geotechnical Journal, **47**: 827–841.

Marchelli, M., Leonardi, A., Pirulli, M., and Scavia, C. 2020. On the efficiency of slit-check dams in retaining granular flows. Géotechnique, **70**(3): 226–237. DOI: 10. 1680/jgeot.18.p.044.

McArdell, B. W., Bartelt, P. and Kowalski, J. 2007. Field observations of basal forces and fluid pore pressure in a debris flow. Geophysical Research Letters, **34**: L07406.

McDougall, S. 2017. 2014 Canadian Geotechnical Colloquium: landslide runout analysis – current practice and challenges. Canadian Geotechnical Journal, **54**: 605–620.

Nagl, G., Hübl, J., and Kaitna, R. 2020. Velocity profiles and basal stresses in natural debris flows. Earth Surface Processes and Landforms, **45**(8): 1764–1776. DOI: 10.1002/esp.4844.

Ng, C. W. W., Choi, C. E. and Law, R. P. H. 2013. Longitudinal spreading of granular flow in trapezoidal channels. Geomorphology, **194**: 84–93.

Ng, C. W. W., Choi, C. E., Goodwin, G. R., Kwan, J. S. H., and Pun, W. K. 2017. Interaction between dry granular flows and deflectors. Landslides, **14**(4): 1375–1387.

Ng, C. W. W., Choi, C. E., Koo, R. C. H., Goodwin, G. R., Song, D. and Kwan, J. S. H. 2018. Dry granular flow interaction with dual-barrier systems. Géotechnique, **68**(5): 1–14.

Ng, C. W. W., Choi, C. E. and Goodwin, G. R. 2019. Froude characterisation for single-surge unsteady dry granular flows: impact pressure and runup height. Canadian Geotechnical Journal, **56**(12): 1968–1978. DOI: 10.1139/cgj-2018-0529.

O'Sullivan. 2011. Particulate Discrete Element Modelling: A Geomechanics Perspective. CRC Press.

Pudasaini, S. P. and Hutter, K. 2003. Rapid shear flows of dry granular masses down curved and twisted channels. Journal of Fluid Mechanics, **495**: 193–208.

Pudasaini, S. P., Hutter, K., Hsiau, S.-S., Tai, S.-C., Wang, Y., and Katzenbach, R. 2007. Rapid flow of dry granular materials down inclined chutes impinging on rigid walls. Physics of Fluids, **19**(5): 053302.

Rycroft, C. H. 2007. Multiscale modelling in granular flow. PhD thesis, MIT, USA.

Salciarini, D., Tamagnini, C., and Conversini, P. 2010. Discrete element modelling of debris-avalanche impact on earthfill barriers. Physics and Chemistry of the Earth, **35**: 172–181.

Salm, B. 1993, Flow, flow transition, and runout distances of flowing avalanches. Annals of Glaciology, **18**: 221–226.

Savage, S. B. and Hutter, K. 1989. The motion of a finite mass of granular material down a rough incline. Journal of Fluid Mechanics, **199**: 177–215.

Scheidl, C., McArdell, B. W. and Rickenmann, D. 2014. Debris-flow velocities and superelevation in a curved laboratory channel. Canadian Geotechnical Journal, **52**: 305–317.

Schraml, K., Thomschitz, B., McArdell, B., Graf, C., and Kaitna, R. 2015. Modeling debris-flow runout patterns on two alpine fans with different dynamic simulation models. Natural Hazards and Earth System Sciences Discussions, **3**(2): 1397–1425. DOI: 10.5194/nhess-15-1483-2015.

Shan, T., and Zhao, J. 2014. A coupled CFD-DEM analysis of granular flow impacting on water reservoir. Acta Mechanica, **225**(8): 2449–2470.

Silbert, L. E., Ertas, D., Grest, G. S., Halsey, T. C., Levine, D. and Plimpton, S. J. 2001. Granular flow down an inclined plane: Bagnold scaling and rheology. Physical Review E, **64**: 051302.

Silbert, L. E., Landry, J. W., and Grest, G. S. 2003. Granular flow down a rough inclined plane: transition between thin and thick piles. Physics of Fluids, **15**(1): 1–10.

Silva, M., Costa, S., Canelas, R. B., Pinheiro, A. N., and Cardoso, A. H. 2016. Experimental and numerical study of slit-check dams. International Journal of Sustainable Development and Planning, **11**(2): 107–118.

Song, D., Choi, C. E., Ng, C. W. W. and Zhou, G. D. D. 2017. Geophysical flows impacting a flexible barrier: effects of solid-fluid interaction. Landslides, **15**: 99–110.

Sovilla, B., Schaer, M., Kern, M., and Bartelt, P. 2008. Impact pressures and flow regimes in dense snow avalanches observed at the Vallée de la Sionne test site. Journal of Geophysical Research: Earth Surface, **113**(F1): F01010. DOI: 10.1029/2006JF000688

Staron, L. and Hinch, E. J. 2005. Study of the collapse of granular columns using two-dimensional discrete-grain simulation. Journal of Fluid Mechanics, **545**: 1–27.

Tai, Y. C., Noelle, S., Gray, J. M. N. T. and Hutter, K. 2001. An accurate shock-capturing finite-difference method to solve the Savage-Hutter equations in avalanche dynamics. Annals of Glaciology, **32**: 263–267.

Tannant, D. D., and Skermer, N. 2015. Mud and debris flows and associated earth dam failures in the Okanagan region of British Columbia. Canadian Geotechnical Journal, **50**(8): 820–833.

Teufelsbauer, H., Wang, Y., Chiou, M.-C., and Wu, W. 2009. Flow-obstacle-interaction in rapid granular avalanches: DEM simulation and comparison with experiment. Granular Matter, **11**(4): 209–220.

Teufelsbauer, H., Wang, Y., Pudasaini, S. P., Borja, R. I., and Wu, W. 2011. DEM simulation of impact force exerted by granular flow on rigid structures. Acta Geotechnica, **6**: 119–133.

Thielicke, W. (2020). PIVlab- particle image velocimetry (PIV) tool (https://www.mathworks.com/matlabcentral/fileexchange/27659-pivlab-particle-image-velocimetry-piv-tool), MATLAB Central File Exchange. Retrieved March 3rd 2020.

Thielicke, W., and Stamhuis, E. J. 2014. PIVlab: towards user-friendly, affordable and accurate digital particle image velocimetry in MATLAB. Journal of Open Research Software 2, Ubiquity Press Ltd.

USGS (United States Geological Survey) 2012. Debris flow, sand, gravel & loam on rough bed (6m^3). https://pubs.usgs.gov/of/2007/1315/videos/2012/2012_08_23.mp4. Link accessed on November 11th 2020.

USGS (United States Geological Survey) 2012. Debris flow over bare bed, sand/gravel mix (10 m^3). https://pubs.usgs.gov/of/2007/1315/videos/2016/2016_06_23.mp4. Link accessed on November 11th 2020.

Vagnon, F. and Segalini, A. 2016. Debris flow impact estimation on a rigid barrier. Natural Hazards and Earth System Sciences, **16**: 1691–1697.

Valentino, R., Barla, G.,and Montrasio, L. 2008. Experimental analysis and micromechanical modelling of dry granular flow and impacts in laboratory flume tests. Rock Mechanics and Rock Engineering, **41**(1): 153–177.

Voellmy, A. 1955. Über die Zerstorungskraft von Lawinen. Schweizerische Bauzeitung, **73**: 212–285.

Wensrich, C. M., and Katterfeld, A. 2012. Rolling friction as a technique for modelling particle shape in DEM. Powder Technology, **217**: 409–417.

Nomenclature

a	Acceleration (DMM)
a_{i}	Proportionality constant
B	Width of the channel (both)
e	Coefficient of restitution (DEM)
E	Elastic modulus (DEM)
E_{bulk}	Bulk elastic modulus (DEM)
Fr	Froude number (both)
$\boldsymbol{F}_{\nabla P}$	Force due to pressure gradient (DMM)
$\boldsymbol{F}_{\rho \boldsymbol{g}}$	Force due to self-weight (DMM)
$\boldsymbol{F}_{\mathrm{T}\mu_{\mathrm{B}}}$	Force due to basal friction (DMM)
$\boldsymbol{F}_{\mathrm{T}\xi}$	Force due to Voellmy term (DMM)
$\boldsymbol{F}_{\mathrm{Total}}$	Total force (DMM)
g	Acceleration due to the Earth's gravity (both)
H_{i}	Height of individual grain (DEM)
H	Flow depth (DEM) / height of boundary block
h	Height of mass block
k_{perm}	Permeability
k	Earth pressure
L	Length of monitoring region (both)
m	Mass of boundary block (DMM)
m_{i}	Mass of a grain (DEM)
N	Number of grains in the monitoring region (DEM)
N_{Sav}	Savage number
P_{x}	x-component of momentum (DEM)
P_{z}	z-component of momentum (DEM)
P_{norm}	Resultant of x- and z- components of momentum (DEM)
S_{C}	Stiffness (compression)
S_{U}	Stiffness (unloading)
t	Time (both)
U_{xi}	x-component of velocity for grain i (DEM)
U_{zi}	z-component of velocity for grain i (DEM)
U_{i}	Velocity of grain i (DEM)
U_{j}	Velocity of grain j (DEM)
U	Bulk flow velocity (both)
V	Flow volume (DMM)
x	Longitudinal displacement of the flow (both)
X_{i}	Longitudinal displacement of boundary block i (DMM)
x_{i}	Longitudinal displacement of mass block i (DMM)
z_{ij}	Vertical displacement between grains i and j
α_{i}	Scattering angle
$\dot{\gamma}$	Shear rate (DEM)
$\dot{\gamma}_{\mathrm{i}}$	Shear rate around ith grain (DEM)
δ	Grain diameter (DEM)
δ_{B}	Grain diameter in the base (DEM)
δ_{F}	Grain diameter in the flow (DEM)
ε	Strain
θ	Slope of the channel (both)
λ	Linear stress

μ	Fluid dynamic viscosity
μ_B	Basal friction angle (both)
ν	Poisson's ratio (DEM)
ν_s	Solid volume fraction
ν_{sol}	Solid volume fraction (DEM)
ξ	Voellmy coefficient (DMM)
ρ	Bulk flow density (both)
ρ_{glass}	Material density of glass (DEM)
σ	Normal stress

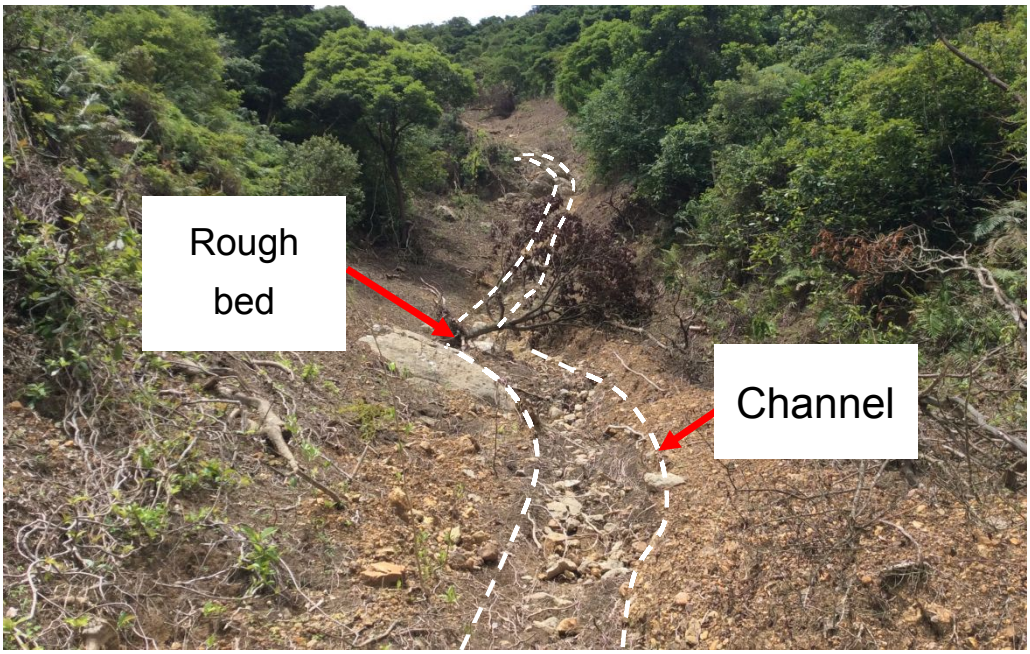

Fig. 1: Rough bed. Photograph taken in Sai Kung, Hong Kong in 2016. (Image modified from Goodwin 2018.)

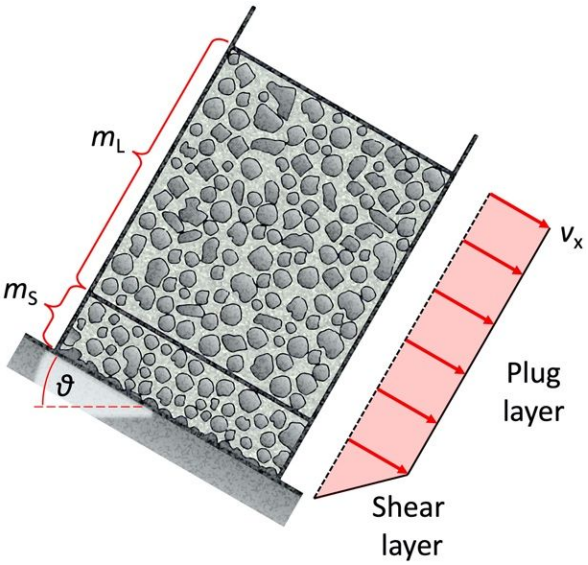

Fig. 2a: Schematic of a shear/plug (dual-layer) flow (after Iverson 1997). m_L is the mass of a plug region; m_s is the mass of the shear layer; and v_x is the local downstream velocity.

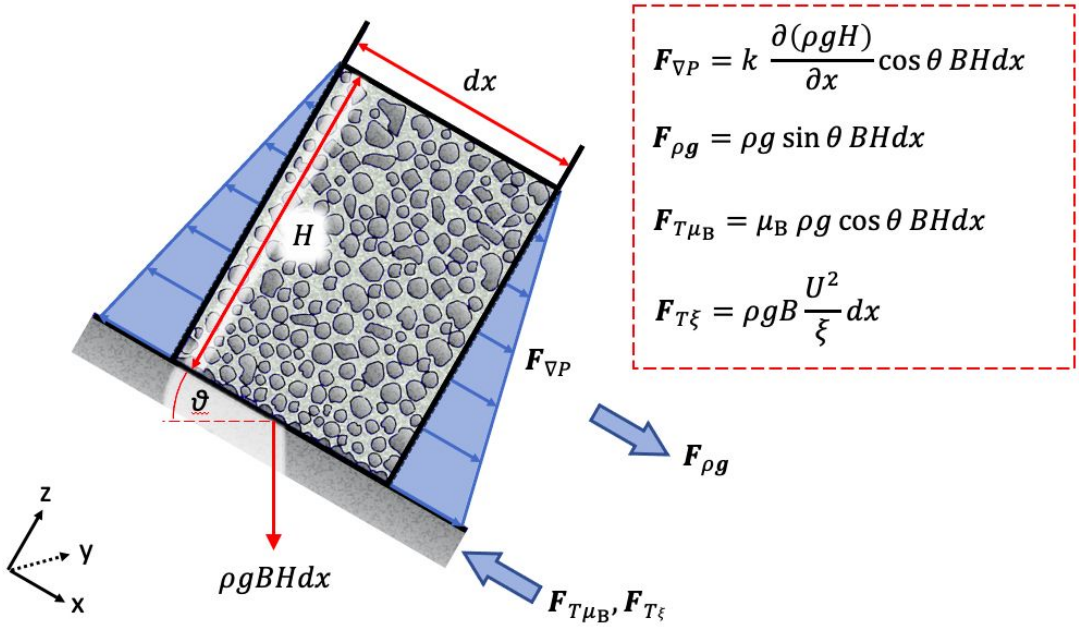

Fig. 2b: Free body diagram of forces considered in an element of a simplified depth-averaged model. Parameters are as follows: $F_{\nabla P}$ is force due to pressure gradient; k is an earth-pressure coefficient; ρ is the bulk density; g is acceleration due to gravity; H is the flow depth; θ is the channel inclination; B is the channel width; dx is the width of the slice; $F_{\rho g}$ is the force due to self-weight; $F_{T\mu B}$ is force due to basal friction; μ_B is the basal friction angle; $F_{T\xi}$ is force due to internal losses; and ξ is a coefficient that describes losses due to internal shearing and granular collisions.

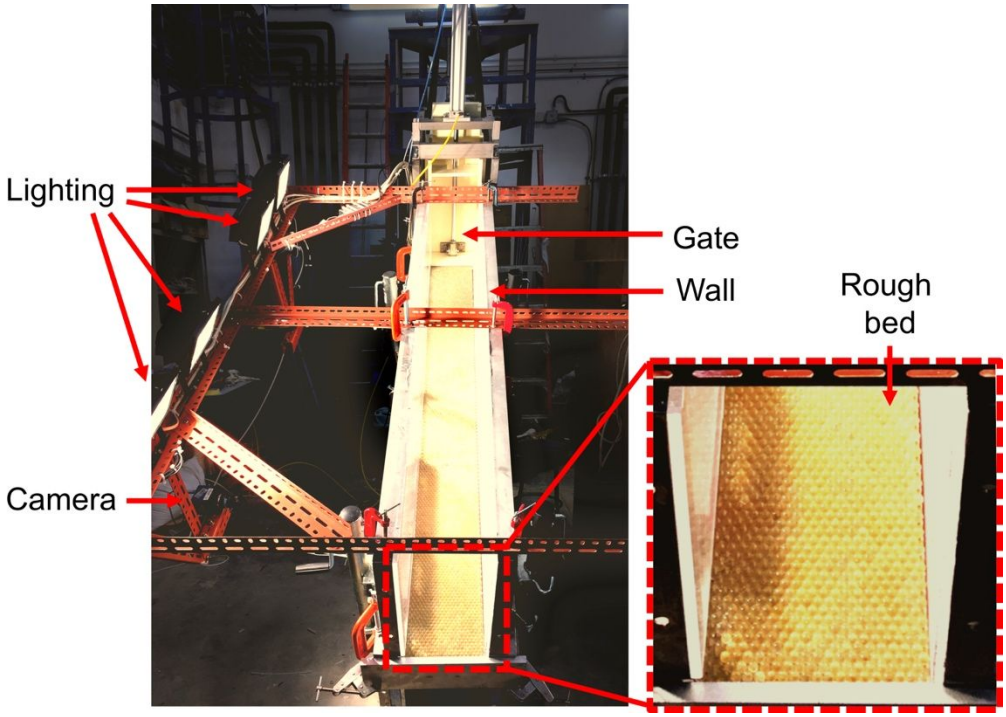

Fig. 3a: Front view of physical flume

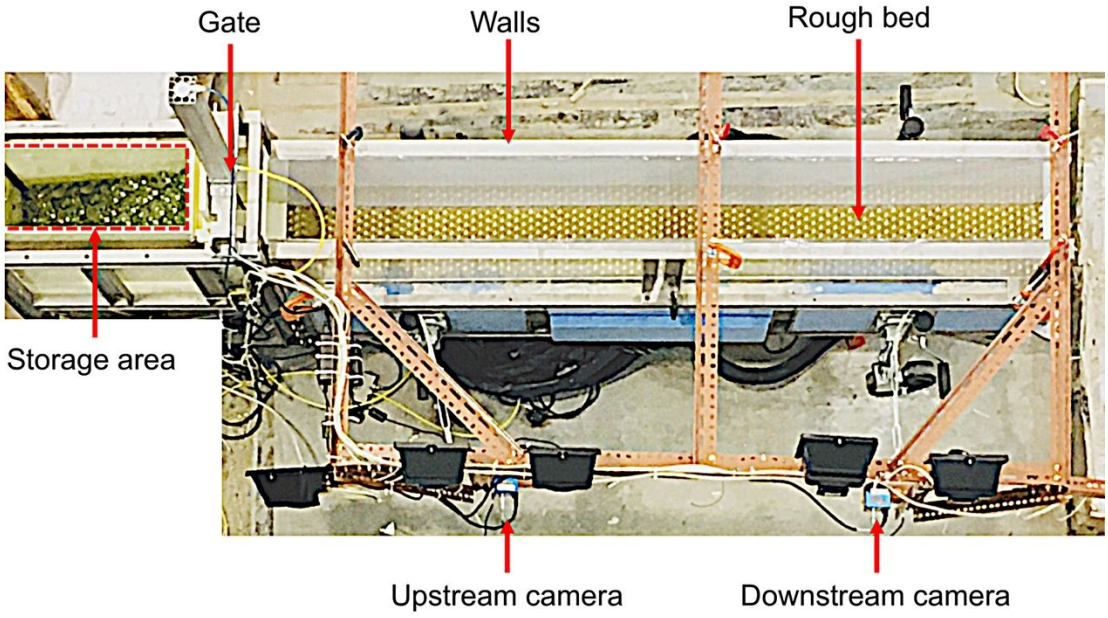

Fig. 3b: Top-down view of physical flume

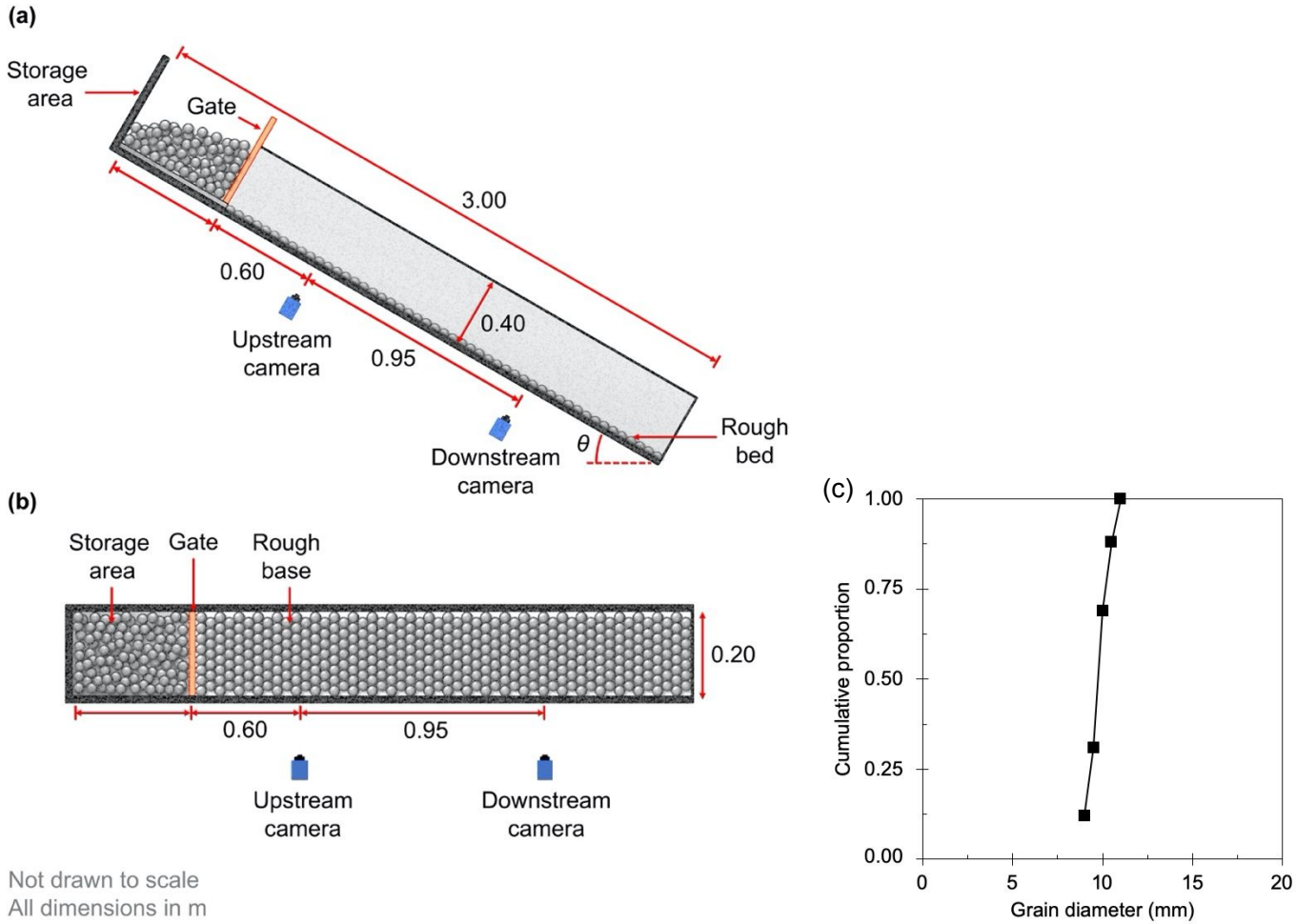

Fig. 4: (a) Side-view schematic of DEM model; (b) top-down view of DEM model; (c) size grading used for the granular material

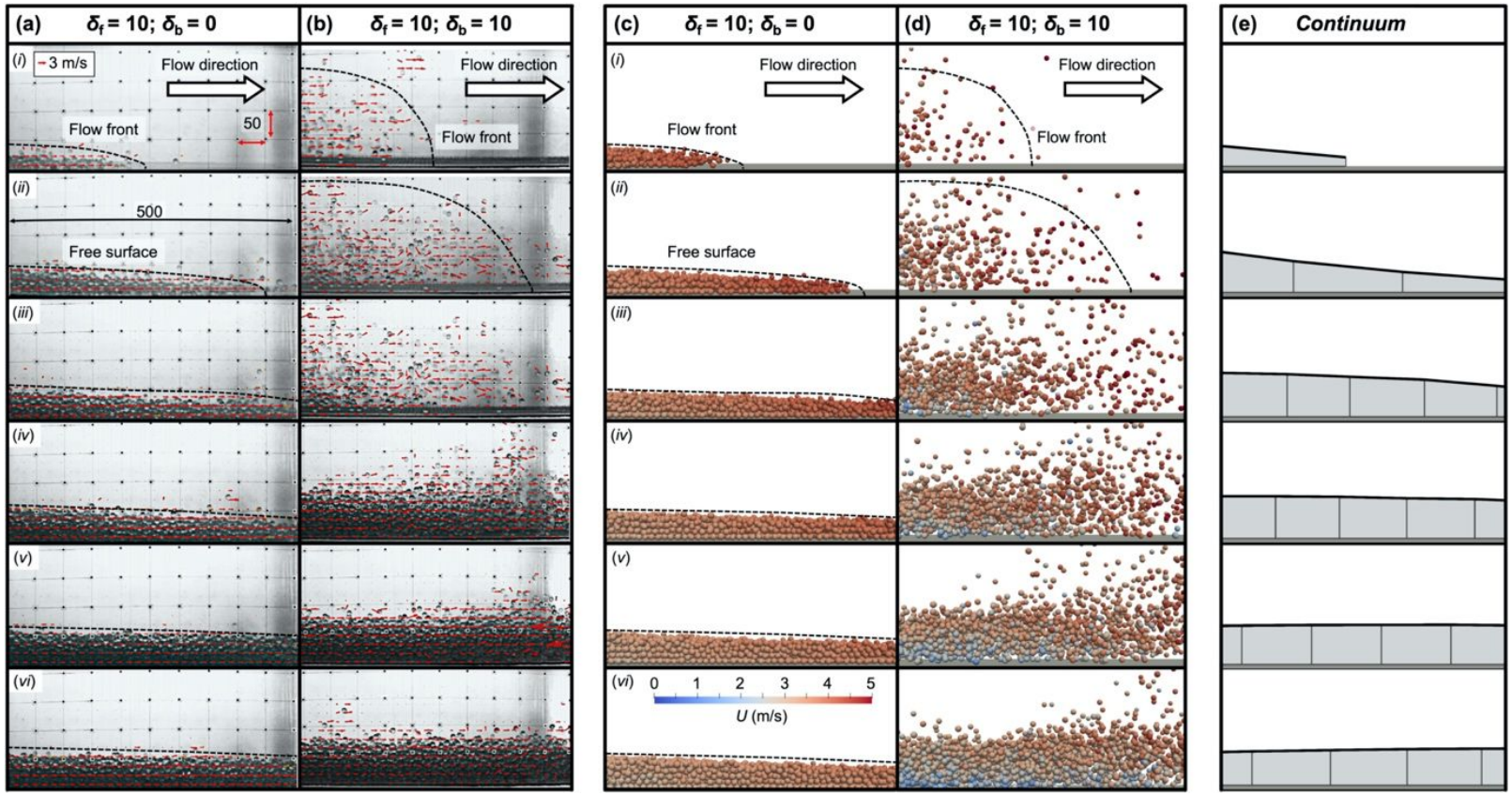

Fig. 5: Comparison of downstream physical and computed flow kinematics. (a) physical, $\delta_B/\delta_F = 0$ (i.e. a smooth bed); (b) physical, $\delta_B/\delta_F = 1$; (c) computed (DEM) $\delta_B/\delta_F = 0$; (d) computed (DEM) $\delta_B/\delta_F = 1$; (e) computed (DMM), for which $\mu_B = 11°$, $\xi = 25$ m/s^2 and $\rho = 1650$ kg/m^3.

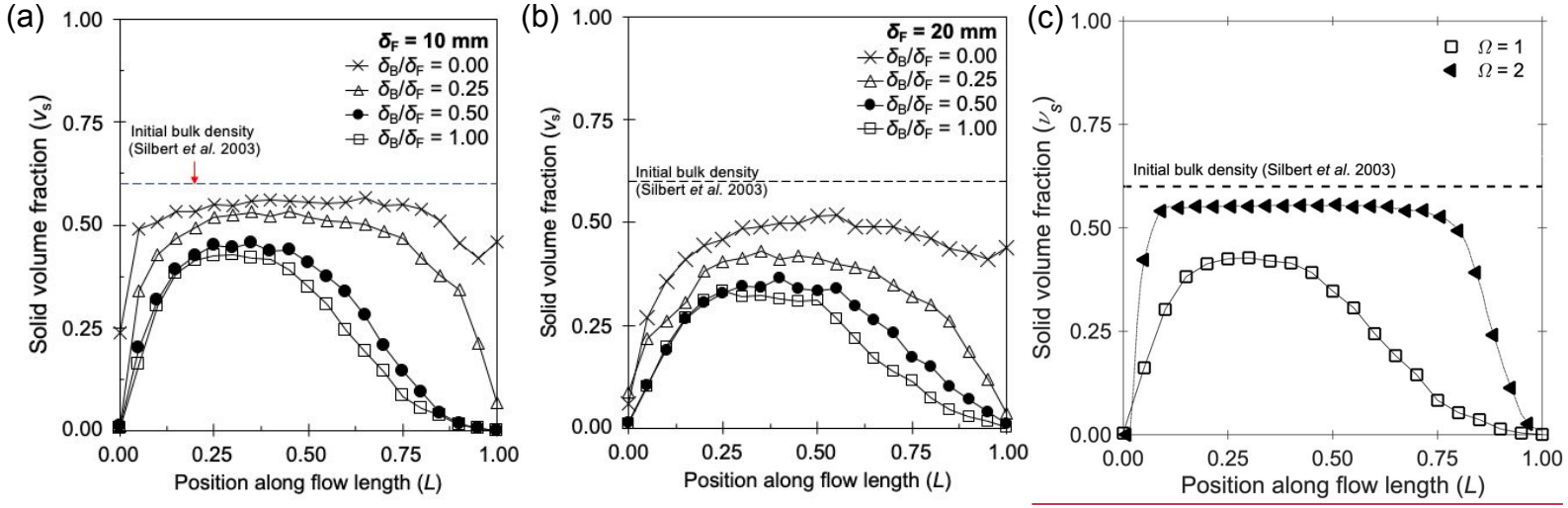

Fig. 6: Solid volume along the length of flows, for different flow grain sizes. (a) δ_F = 10 mm; (b) δ_F = 20 mm. Part (c) shows the same ratio of δ_B/δ_F = 1.00 for two different scales: Ω = 1 and 2, where Ω is a geometric scaling factor applied to the dimensions of the flume and the total volume of the material. δ_F is held constant at 10 mm for both values of Ω.

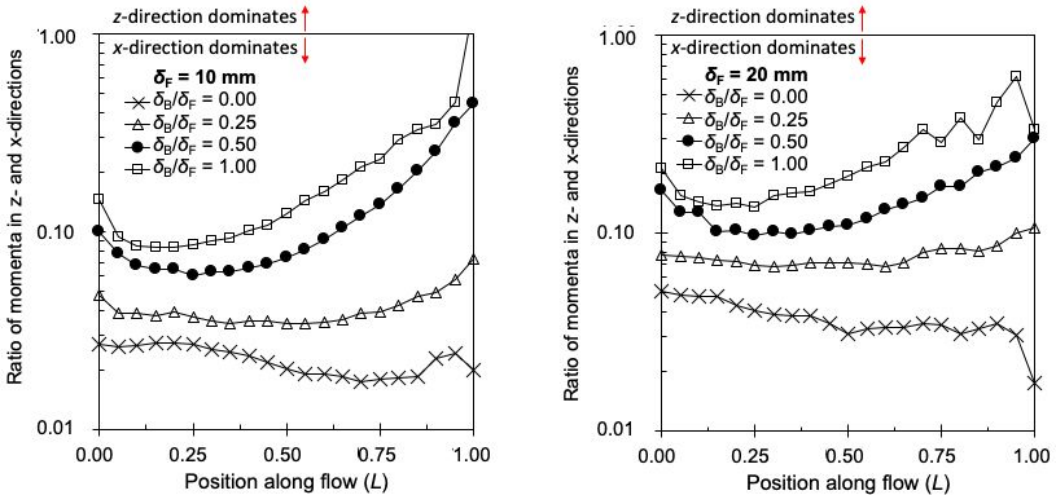

Fig. 7: Momentum along the length of flows, for different flow grain sizes. (a) δ_F = 10 mm; (b) δ_F = 20 mm

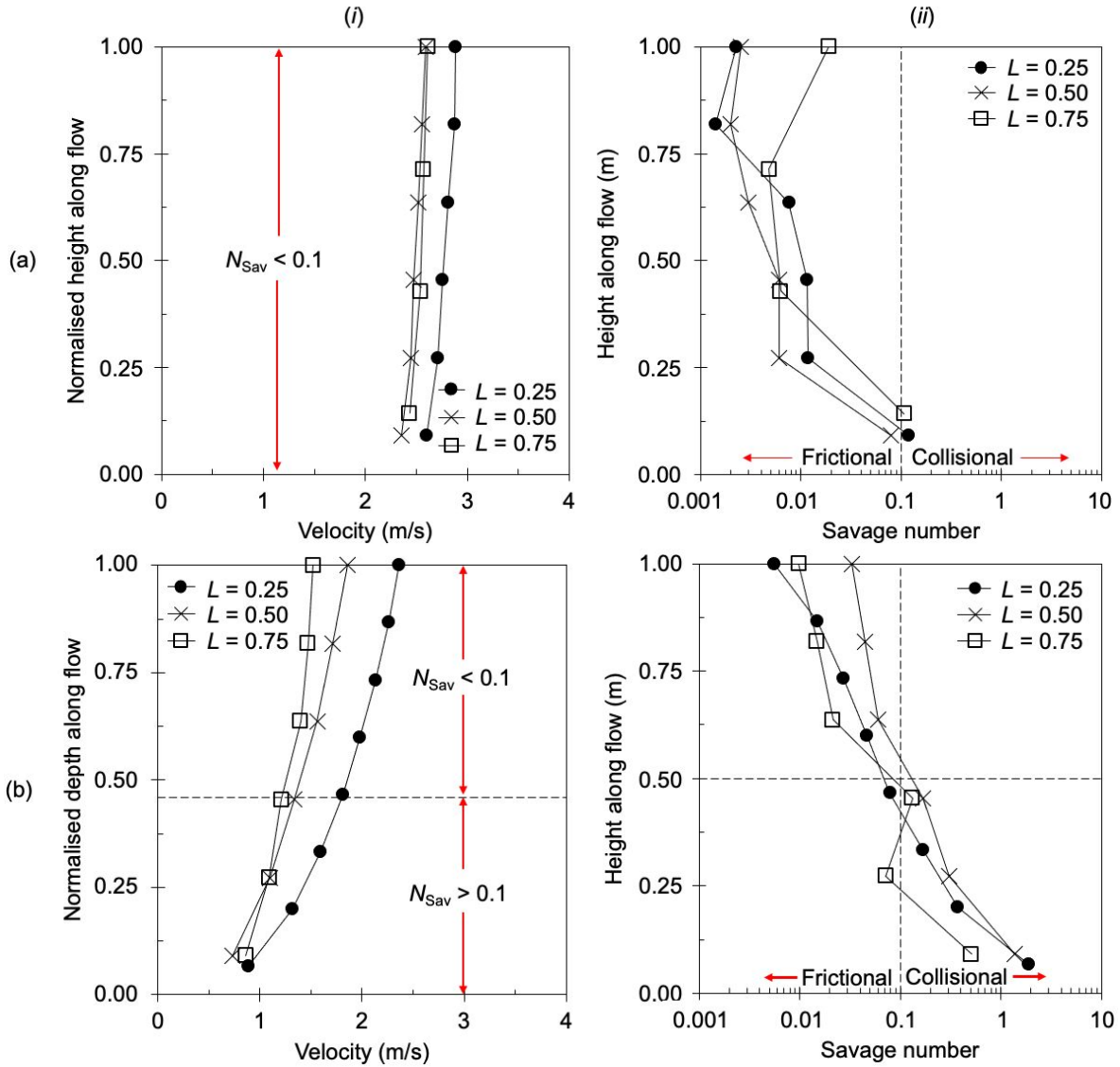

Fig. 8: Comparison of velocity profiles and Savage number, where δ_B = 10 mm. (*a*) δ_B/δ_F = 0; (*b*) δ_B/δ_F = 1

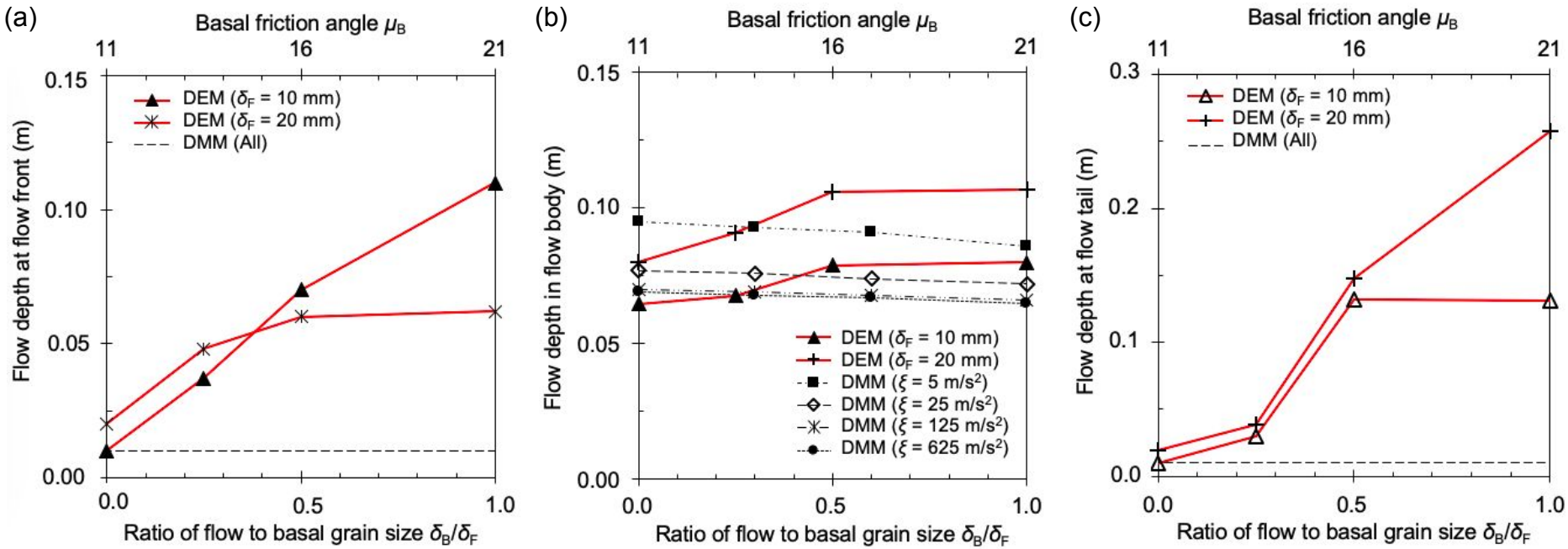

Fig. 9: Comparison of the flow depth at (a) the front, (b) the body and (c) the tail of the flow, for both the DEM and DMM.

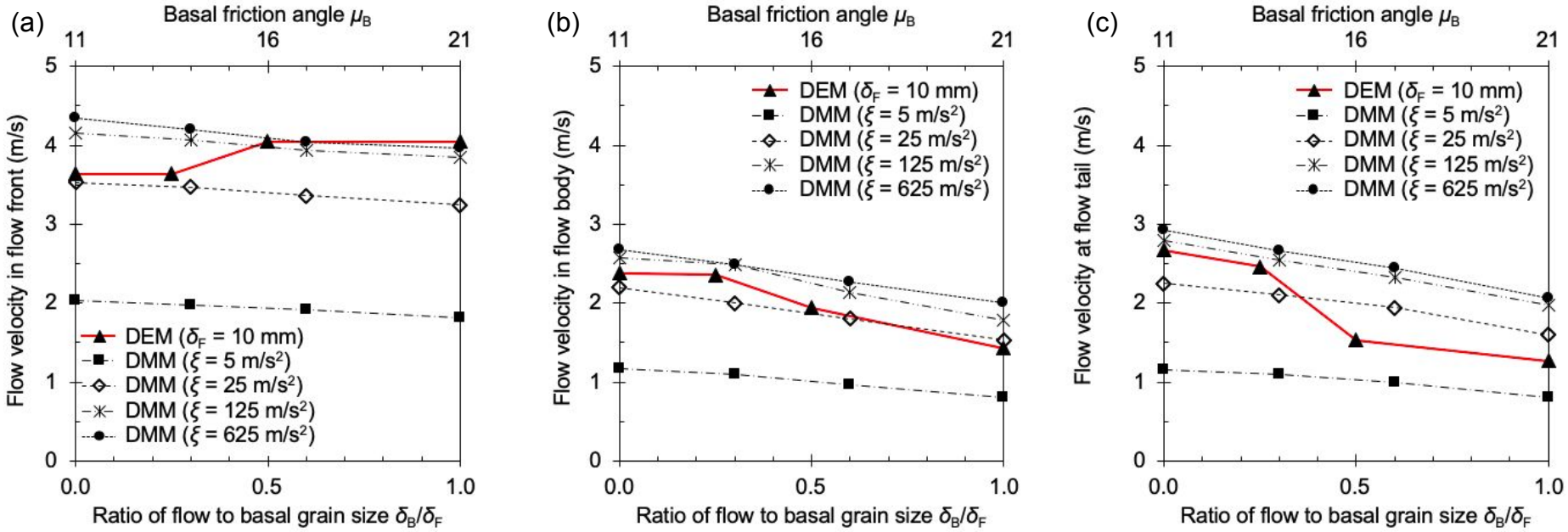

Fig. 10: Comparison of the flow velocity at (a) the front, (b) the body and (c) the tail of the flow, for both the DEM and DMM.

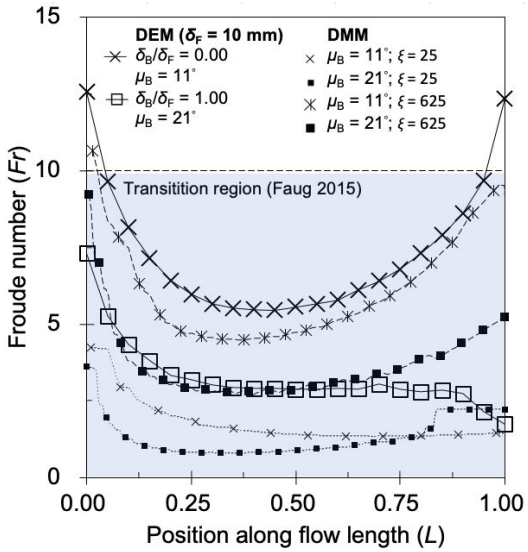

Fig. 11: Froude number along the length of flows, for both the DEM and the DMM.

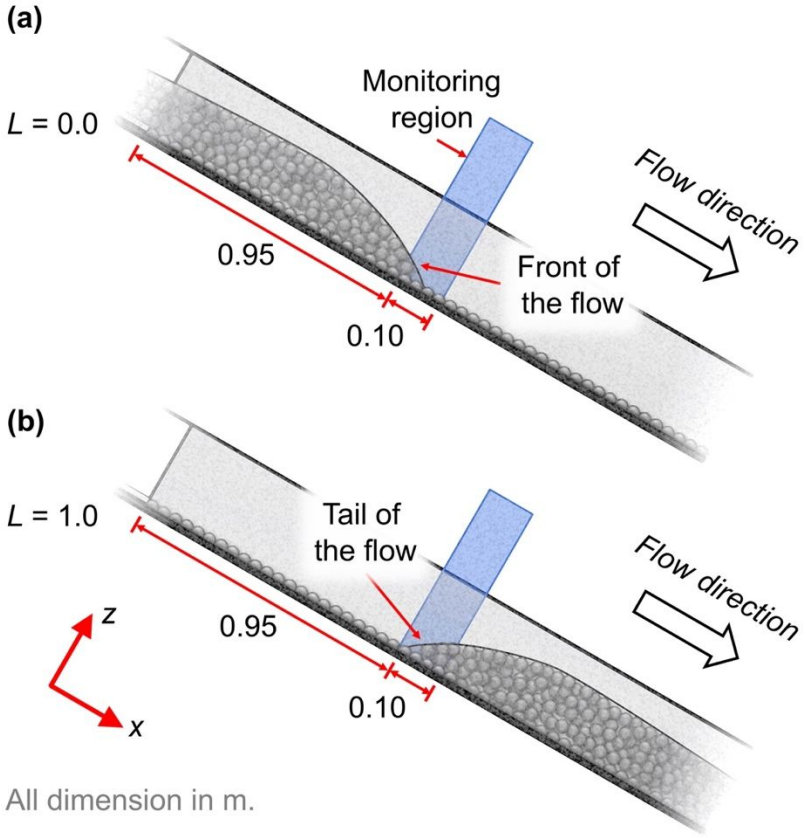

Fig. A1: Definition of monitoring region & quantity *L* ("normalised position along flow length").

Fig. C1: comparison of the angular gravel and the glass beads

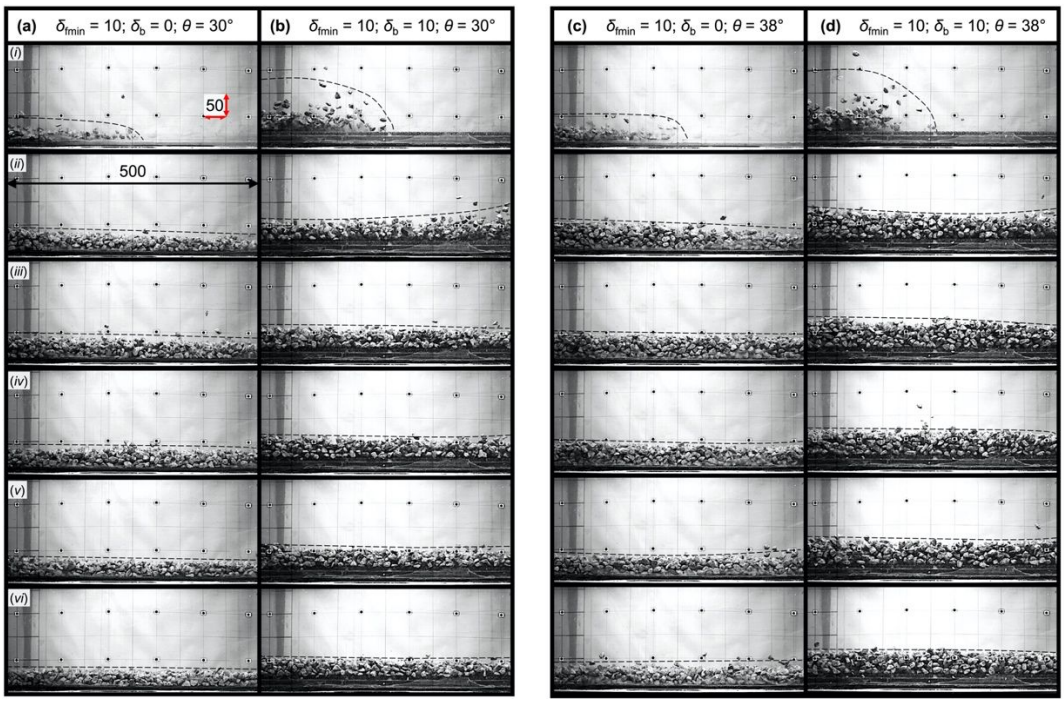

Fig. C2: Flow kinematics for angular gravel: (a) θ = 30°, smooth bed condition; (b) θ = 30°, rough bed condition; (c) θ = 38°, smooth bed condition; (b) θ = 38°, rough bed condition. Frames are separated by 0.2 s: (*i*) 0.0 s; (*ii*) 0.2 s; (*iii*) 0.4 s; (*iv*) 0.6 s; (*v*) 0.8 s; (*vi*) 1.0 s.

Tables

Table 1: Parameters adopted in numerical simulations

	DEM simulations	**DMM simulations**
Total mass of material (kg)	40	40
Diameter (m)	0.010 ± 0.001	-
Material density (kg/m^3)	2650	-
Bulk density (kg/m^3)	-	1650
Internal friction angle (°)	19.8	-
Interface friction angle (°)	16.6	11 to 21
Young's modulus (Pa)	10^8	-
Poisson's ratio	0.3	-
Rolling resistance	0	-
Contact model	Hertzian	-
Coefficient of restitution	0.93	-
Earth pressure coefficient	-	Incremental (Hungr 1995)
Voellmy coefficient ξ (m/s)	-	5 – 625

Table 2: Test plan

	No. of tests	**Material**	**Channel inclination** θ (°)	**Flow grain size** δ_F (mm)	**Flow to basal grain size ratio** $\delta_B/\ \delta_F$	**Voellmy coefficient** μ_b	**Voellmy coefficient** ξ (m/s)	**Geometric scaling factor Ω**
Physical tests	2	Glass beads	30	10	0.00, 1.00	-	-	1
	4	Angular gravel	30, 38	~10	0,00, 1.00	-	-	1
DEM simulations	8	-	30	10, 20	0.00, 0.25, 0.50, 1.00	-	-	1
	2			10	1.00	-	-	1, 2
DMM simulations	16	-	30	-	-	11, 14, 17, 21	5, 25, 125, 625	1

Table C1: Summary of velocities, depths and *Fr* numbers for the gravelly flows.
The velocities were extracted using OpenPIV (Thielicke and Stamhuis 2014).

Bed condition	**Inclination** (°)	**Max. frontal velocity** (m/s)	**Max. body velocity** (m/s)	**Estimated max. body depth** (m)	**Estimated body Froude**
Rough	30	1.7	1.1	0.03	2.1
Smooth	30	2.1	1.6	0.03	3.2
Rough	38	2.3	2.0	0.05	3.2
Smooth	38	2.6	2.3	0.04	4.1

Appendix A

Discrete element modelling: scaling and data extraction

For the extracted quantities, we use a monitoring region that covers the entire width and height of the channel. The centroid of the monitoring region is positioned at x = 1 m; its length in the x-direction is 0.1 m for the DEM tests (but 0.5 m for the DMM tests, because of sampling issues that otherwise arise due to a small number of boundary blocks). We use the monitoring region to define L, which is the normalised position along the flow length. L is zero when the flow front enters the monitoring region, and unity when the tail of the flow leaves the monitoring region (see Fig. A1).

The flow depth H is calculated as twice the mean of the z-positions of the grains in the monitoring section:

$$H = \frac{2}{N}\sum_{i=1}^{N} h_{\mathrm{i}} \tag{A1}$$

where i denotes individual grains and N is the total number of grains in the monitoring region.

The bulk velocity is the mean of the velocities of each grain:

$$U = \frac{1}{N}\sum_{i=1}^{N} U_{\mathrm{i}} \tag{A2}$$

The Froude number (Fr) describes the balance of inertial and gravitational stresses in a flow and is important for scaling (Ancey 2001; Armanini and Larcher 2001; Armanini et al. 2011, 2014; Armanini 2015; Kesseler et al. 2018). Fr and our sampling method are given as:

$$Fr = \frac{U}{\sqrt{gH}} \tag{A3a}$$

$$Fr = \frac{1}{N}\sum_{i=1}^{N} \frac{U_{\mathrm{i}}}{\sqrt{gh_{\mathrm{i}}}} \tag{A3b}$$

(Note: Eqn. (A3a) is identical to Eqn. (4), but we repeat it here for convenience.)

The solid volume fraction is another governing parameter for granular flow dynamics (Bagnold 1954; Armanini et al. 2011, 2014; and Armanini 2013, 2015), and is calculated as:

$$\nu_{\mathrm{sol}} = \frac{N\pi\delta^3}{6LHB} \tag{A4}$$

where N is the number of grains in the measuring region; δ is the grain diameter; L is the length of the measuring region; H is the flow depth; and B is the channel width.

Macroscopically rough bases transfer momentum away from the channel-parallel direction. To quantify this effect, we divide the base-perpendicular momentum (P_z) by the downstream (P_x) momentum for each grain:

$$P_{\text{norm}} = \frac{P_z}{P_x} = \frac{\sum_{i=1}^{N} m_i |U_{xi}|}{\sum_{i=1}^{N} m_i |U_{zi}|} \tag{A5}$$

where m_i is the mass of each grain.

The Savage number (Iverson 1997) describes the ratio of frictional and collisional stresses locally in a flow, and indicates whether the flow exhibits shear or plug behaviour (Fig. 2a). The Savage number and its calculation in the DEM are:

$$N_{\text{Sav}} = \frac{\delta^2 \dot{\gamma}^2}{gH} \tag{A6a}$$

$$N_{\text{Sav}} = \frac{1}{N} \sum_{i=1}^{N} \frac{\delta^2 \dot{\gamma_i}^2}{g h_i} \tag{A6b}$$

where $\dot{\gamma}$ is the shear rate and is equal to $(U_j - U_i)/z_{ij}$. The subscript j indicates another grain in the vicinity and z_{ij} is the vertical displacement between them.

Appendix B

Our DMM model is based on that described by Hungr (1995). It solves the Navier-Stokes equation for incompressible fluids, which states that motion of the equivalent fluid is driven by the pressure gradient and self-weight of the flow:

$$\rho V\left(\frac{\partial \boldsymbol{U}}{\partial t}\right) = \boldsymbol{F}_{\nabla P} + \boldsymbol{F}_{\rho \boldsymbol{g}} - \left(\boldsymbol{F}_{\mu_{\mathrm{B}}} + \boldsymbol{F}_{\xi}\right) \tag{B1}$$

where ρ is bulk density; V is volume; U is velocity; t is time; $F_{\nabla P}$ is force due to the pressure gradient; $F_{\rho g}$ is force due to self-weight; $F_{\mu B}$ is force due to basal friction; and F_{ξ} is a lumped force that accounts for energy dissipation due to internal processes such as frictional shearing and inelastic collisions. Pressure is assumed to be hydrostatic, so P is given by $k\rho gH$, where k is the earth pressure coefficient.

Force terms are calculated as follows (Hungr 1995):

$$\boldsymbol{F}_{\nabla P} = k\frac{\partial(\rho \mathbf{g} H)}{\partial x} H\cos\theta B dx \tag{B2a}$$

$$\boldsymbol{F}_{\rho \boldsymbol{g}} = \rho \mathbf{g} H \sin\theta B dx \tag{B2b}$$

$$\boldsymbol{F}_{\mu_{\mathrm{B}}} = -\left(\frac{\boldsymbol{U}'}{|\boldsymbol{U}|'}\right)\rho g H \cos\theta \mu_{\mathrm{B}} B dx \tag{B2c}$$

$$\boldsymbol{F}_{T\xi} = -\left(\frac{\boldsymbol{U}'}{|\boldsymbol{U}|'}\right)\rho g \frac{U^2}{\xi} B dx \tag{B2d}$$

where H is the height of the boundary block, B is the width of the channel, dx is the width of the boundary block; and the dash indicates the previous timestep. The terms ξ and μ_{B} are Voellmy coefficients that quantify energy loss due to "turbulence" and the basal friction angle, respectively. (In this manuscript, we interpret ξ as accounting for losses due to grain collisions and internal frictional shearing.) The term -($\boldsymbol{U}'/|\boldsymbol{U}'|$) is a unit vector that makes resisting forces oppose the direction of motion. These forces are shown schematically in Fig. 2b.

As for the definition of k (in Eqn. B2a), the formulation proposed in Hungr (1995) was adopted. The coefficient k indicates the lateral pressure and depends on strain and is initially unity. It is defined as being the ratio between the tangential and normal stresses in the flowing mass of material. It is calculated for the boundary blocks (subscripted with i) and for the mass blocks (subscripted with j). An averaging process is used to find the longitudinal pressure gradient at each boundary block; it is given as the average for the two adjacent mass blocks:

$$k_{\mathrm{i}}\frac{dH}{ds} = \frac{1}{2}\left[\frac{k_{\mathrm{j}}(h_{\mathrm{j}} - H_{\mathrm{j}})}{x - X_{\mathrm{i}}} + \frac{k_{\mathrm{j}-1}(H_{\mathrm{j}} - h_{\mathrm{j}-1})}{X_{\mathrm{i}} - x_{\mathrm{j}-1}}\right] \tag{B3}$$

where H is the height of the boundary blocks; h is the height of the mass blocks; X is the displacement of the boundary blocks; and x is the displacement of the mass blocks. The incremental tangential strain $\Delta\varepsilon_j$ for each of the mass blocks is then computed using the displacements of adjacent boundary blocks.

$$\Delta\varepsilon_j = \frac{(X_{i+1} - X_i) - (X'_{i+1} - X'_i)}{X'_{i+1} - X'_i} \tag{B4}$$

where the dash indicates a value from the previous timestep. The strain is then used to update k at the current timestep:

$$k_j = k'_j + S_c \Delta\varepsilon_j \tag{B5}$$

where S_c is a compressional stiffness coefficient for each block, although S_u, a stiffness coefficient for unloading, can also be used. The value k_j is then used to update S_c and S_u:

$$S_c = \frac{k_p - k_a}{0.05} \qquad S_u = \frac{k_p - k_a}{0.025} \tag{B6}$$

Displacements are calculated based on these forces using Newton's laws of motion.

$$a = \frac{\boldsymbol{F}_{\text{Total}}}{m} = \frac{\boldsymbol{F}_{\nabla P} + \boldsymbol{F}_{\rho \boldsymbol{g}} - (\boldsymbol{F}_{T1} + \boldsymbol{F}_{T2})}{\rho H B dx} \tag{B7a}$$

$$U = U' + a\, dt \tag{B7b}$$

$$x = x' + U\, dt + \frac{1}{2} a\, dt^2 \tag{B7c}$$

where a, U, x and m are the acceleration, velocity, displacement and mass of the boundary block. One difference with the model described in Hungr (1995) is that we also apply a boundary condition perpendicular to the channel base to model the far end of the storage container.

$$\begin{aligned} &\text{if } x_i < -0.439 \text{ m}, \\ &\quad x_i = -0.439 \text{ m} \\ &\quad U_i = 0 \text{ m/s} \end{aligned} \tag{B8}$$

This prevents material spreading upstream. No mesh entanglement was observed as a consequence of this boundary condition. Finally, although our implementation is able to account for lateral spreading, we set acceleration in this direction to be zero. This is because the physical and DEM tests both consider a rectangular channel with a constant width.

For all simulations, the density for the equivalent fluid was set to be 1650 kg/m^3, the same as the nominal bulk density for dense flows of monodisperse glass beads.

Appendix C

To ensure that the glass beads were reasonably representative of the dynamics of flows comprising real geological materials, a set of physical tests were performed using angular gravel. The gravel was sieved through a square mesh with an opening of 11 mm, meaning that the gravel was similarly sized to the glass beads which had a nominal diameter of 10 mm. A total mass of 40 kg of gravel was prepared. A comparison of the gravel used and the glass beads is shown in Fig. C1. The experimental procedure was the same as for the glass beads. Two basal conditions were used: a smooth base, and the base comprising a hexagonal lattice of 10 mm glass beads. Two channel inclinations were used, specifically 30° and 38°. This allowed *Fr* to be varied to cover the range for the tests with the glass beads (since properties of the gravel such as the angularity and the coefficient of restitution tend to cause relative retardation of the flow).

Fig. C2 shows the flow kinematics for the angular gravel. The images are scaled so that they are the same size as in Fig. 5 in the main paper. The region of the flume being observed is also the same (centred at 1.55 m downstream). The kinematics for the two cases on the smooth bed (Figs. C2a and C2c) show that a dense, tapered front reminiscent of the flows of glass beads on smooth beds can be achieved. The maximum flow depths are around 0.05 m for both cases, which again is similar to the maximum depths for the flows of glass beads (Fig. 5).

Figs. C2b and C2d show the kinematics for the gravelly flows on rough beds. As with the flows of glass beads on rough beds, the flow front is noticeably more dispersed than the corresponding flows on the smooth bed. Nonetheless, the degree of dispersion is noticeably less than that of the glass bead flows. Furthermore, the dispersion is suppressed by the depth of the flow sooner than for the glass beads. This is likely due to a combination of factors, including the coefficient of restitution and the angularity of the gravel.

Nonetheless, the degree of dispersion for angular gravel is still reminiscent of the flows of spheres on intermediate basal conditions (see the computed bulk flow densities for different basal conditions given in Fig. 6). Furthermore, dispersed flow fronts for flows including gravel have also been observed at larger scales (see USGS 2012 and 2016 for roughened and smooth beds, respectively). This provides a useful context for interpreting the results from the tests using glass beads: smaller (but nonetheless nonzero) basal roughnesses are likely to be most representative of field conditions. Table C1 summarises information about the flow depth, velocity and Froude number.